NASA TECHNICAL NOTE

NASA TN D-2900

NASA TN D-2900

FACILITY FORM 602

N65-28636 (ACCESSION NUMBER)
(THRU)
64 (PAGES)
1 (CODE)
(NASA CR OR TMX OR AD NUMBER)
01 (CATEGORY)

GPO PRICE $
CFSTI
~~OTS~~ PRICE(S) $ 3.00

Hard copy (HC)
Microfiche (MF) .75

EFFECT OF NOSE BLUNTNESS AND CONTROLLED ROUGHNESS ON THE FLOW ON TWO HYPERSONIC INLET CENTER BODIES WITHOUT COWLING AT MACH 5.98

by James M. Cubbage

Langley Research Center
Langley Station, Hampton, Va.

NATIONAL AERONAUTICS AND SPACE ADMINISTRATION • WASHINGTON, D. C. • JULY 1965

NASA TN D-2900

EFFECT OF NOSE BLUNTNESS AND CONTROLLED ROUGHNESS ON THE FLOW ON TWO HYPERSONIC INLET CENTER BODIES WITHOUT COWLING AT MACH 5.98

By James M. Cubbage

Langley Research Center
Langley Station, Hampton, Va.

NATIONAL AERONAUTICS AND SPACE ADMINISTRATION

For sale by the Clearinghouse for Federal Scientific and Technical Information
Springfield, Virginia 22151 – Price $3.00

EFFECT OF NOSE BLUNTNESS AND CONTROLLED ROUGHNESS ON THE FLOW ON TWO HYPERSONIC INLET CENTER BODIES WITHOUT COWLING AT MACH 5.98

By James M. Cubbage
Langley Research Center

SUMMARY

28636

Results from an experimental investigation of nose bluntness and controlled roughness effects on the pressure recovery, on the location of transition, and on boundary-layer development on two center bodies for an all-external-compression hypersonic inlet are presented. The models were bodies of revolution having a conical forepart followed by an isentropic compression surface. The center-body models differed only in the cone half-angle, one being 10° and the other 20°. Equilibrium surface temperatures and surface static pressures were measured on these center bodies for nose radii of 0 to 0.45 inch and roughness sizes of 0.031- to 0.063-inch diameter at a free-stream Mach number of 5.98. The corresponding free-stream Reynolds number was 7×10^6 per foot and all data were obtained at zero angle of attack. Total-pressure surveys of the boundary layer were made at two locations on each model.

The data show that nose blunting and roughness size had only a small effect on model surface pressures. Increasing the nose radius from 0 to 0.14 inch increased the transition Reynolds number substantially. Further increases in nose radius had little or no effect on this parameter. The roughness size necessary to fix transition at the roughness location on the forebody having a 10° semiapex angle was found to exceed the boundary-layer thickness at this location by a factor of about 2. Boundary-layer momentum and displacement thickness generally increased with increasing nose radius.

INTRODUCTION

The practical design of an inlet for a hypersonic air-breathing propulsion system must compromise some of the aerodynamic requirements to satisfy necessary structural requirements. For example, some initial turning of the flow by a wedge or cone is required to reduce the length of the inlet to make it structurally feasible. Also, some blunting of leading edges will be required to accommodate coolant passages or to provide strength for high-temperature materials. It has been shown (refs. 1 to 6, for example) that blunting of the leading edge or nose delays transition of the boundary layer on downstream surfaces. This delay in transition could lead to separation of the flow on the compression surfaces following the initial wedge or conical surfaces and thus affect inlet performance. Consequently, a boundary-layer trip may be necessary to establish transition upstream from these surfaces.

The present investigation was initiated to determine the effects of nose bluntness on boundary-layer transition and growth and on the pressures on the center body of an external compression inlet designed for Mach 6. The effect on boundary-layer development of fixing transition at a forward location on the center body was also investigated. The two center-body models investigated had conical forebodies with semiapex angles of 10° and 20° followed by an isentropic compression surface. The total flow-turning angle on both models was about 36° and the nose radius of each model was varied from 0 to 0.45 inch. The location of transition was determined from surface temperature distributions supplemented by schlieren photographs. Total-pressure surveys of the boundary layer were made at two locations on each model.

The investigation was conducted in the Langley 20-inch Mach 6 tunnel at zero angle of attack and at a free-stream Reynolds number of 7×10^6 per foot. All data were obtained at equilibrium wall temperatures. The Reynolds number based on the model inlet diameter (approximately 6.1×10^6 for the 10° model and 6.3×10^6 for the 20° model) corresponded to that for a 6-foot-diameter Mach 6 inlet operating at an altitude of 90,000 feet.

SYMBOLS

k	roughness height, in.
M	Mach number
p	pressure, psia
$\frac{p_w}{p_{t,0}}$	ratio of wall static pressure to tunnel stagnation pressure
R_b	bluntness Reynolds number, $\left(\frac{u}{\nu}\right)_\infty \frac{2r_n}{12}$
R_k	roughness Reynolds number, $\left(\frac{u}{\nu}\right)_\delta \frac{k}{12}$
R_{tr}	transition Reynolds number, $\left(\frac{u}{\nu}\right)_\delta \frac{s_{tr}}{12}$
R_θ	Reynolds number based on momentum thickness, $\left(\frac{u}{\nu}\right)_\delta \frac{\theta}{12}$

r_n	model nose radius, in.
s	distance along model surface as measured from the tip of the nose, in.
T	temperature, °R
$\frac{T_w}{T_t}$	ratio of equilibrium wall temperature to tunnel stagnation temperature
u	velocity, ft/sec
x	distance along model center line from apex of conical forebody, in.
x'	distance along model center line from nose of model, in.
y	distance perpendicular to, and measured from, model center line, in.
y_s	distance perpendicular to, and measured from, model surface, in.
δ	boundary-layer thickness, in.
δ^*	boundary-layer displacement thickness, $\int_0^\delta \left(1 - \frac{\rho u}{\rho_\delta u_\delta}\right) dy_s$, in.
θ	boundary-layer momentum thickness, $\int_0^\delta \left(1 - \frac{u}{u_\delta}\right)\frac{\rho u}{\rho_\delta u_\delta}\, dy_s$, in.
ν	kinematic viscosity, sq ft/sec
ρ	density, slugs/cu ft
σ	semiapex angle of conical forebody, deg

Subscripts:

aw	adiabatic wall
lam	laminar
t	total
tr	transition
turb	turbulent
w	wall or model surface
δ	outer edge of boundary layer

∞	free-stream conditions
0	conditions in tunnel settling chamber
1	conditions downstream of oblique shock
2	conditions downstream of normal shock

APPARATUS AND METHODS

Tunnel

This investigation was conducted in the Langley 20-inch Mach 6 tunnel at a stagnation pressure of 365 psia and at a stagnation temperature of 400° F; the corresponding Reynolds number was 7×10^6 per foot. The Langley 20-inch Mach 6 tunnel is an intermittent type exhausting to atmospheric pressure and has a fixed two-dimensional nozzle block that forms an approximately 20-inch-square test section. Tunnel operating times for the conditions of this investigation were on the order of 20 minutes. A drawing and further details of the tunnel may be found in reference 7.

Models and Supports

Models.- Drawings of the two inlet center-body models along with tables of surface coordinates and instrumentation locations are presented in figure 1. The center-body models were essentially half-models mounted on a combination splitter and mounting plate. Only about the first half of each model was retained as a full body of revolution. This arrangement permitted larger diameter models to be used in the tunnel than would have been possible had a complete model been used.

The contours of the two models were made up of a conical forebody followed by an isentropic compression surface that terminated in a short conical section. The latter portion faired into the rounded shoulder at the rear of the model. The isentropic section of the $\sigma = 10^\circ$ model turned the flow 25.4° in addition to the initial 10° turning by the conical forebody. The total flow-turning angle on the $\sigma = 20^\circ$ model was 35.9°. The coordinates for an imaginary cowl lip are listed in figure 1 for the two models. This cowl lip was the inviscid-flow focal point on the sharp-nosed configurations for the conical shock and the Mach lines generated by the isentropic compression surface. No correction was made to the compression surface contour to account for boundary-layer growth. Both center-body models were investigated with nose radii of 0, 0.14, 0.28, and 0.45 inch. These radii correspond to about 1, 2, and 3 inches on a 6-foot-diameter inlet. Photographs of the two models and the interchangeable nosepieces are presented in figure 2.

The models were fabricated of fiber glass and an epoxy resin and, except for the stainless-steel nosepiece, were hollow with a wall thickness of approximately 0.1 inch. The actual contour of the models differed by a maximum of ±0.015 inch from the specified contour with an average deviation of about ±0.007 inch. The models were mounted in the tunnel by means of a fixed rearward strut and a remotely adjustable forward strut. (See fig. 1(b).) The rearward strut was hollow to permit routing of all pressure and thermocouple leads to the outside of the tunnel.

Boundary-layer trips.- Boundary-layer trips employed in this investigation consisted of steel spheres spot-welded to a 3/8-inch-wide by 0.0015-inch-thick band of an iron nickel alloy. (See fig. 2(c).) This band was attached to the model by silicone rubber cement. The steel spheres had diameters of 0.031, 0.047, and 0.063 inch and were mounted on the band with a center-to-center spacing of 4 diameters. The band was attached to the model in such a manner that one of the spheres was in line with static pressure orifices and thermocouples installed along a meridian of the model. The number of spheres used for each roughness configuration varied with the diameter of the sphere. In no case, however, did the spheres span less than a 60° segment of the model cross section. To provide a greater weld area for greater strength, a small flat was ground on the 0.063-inch-diameter spheres. This flat reduced the height of these spheres 0.005 inch. The silicone rubber cement used to attach the metal band to the model added approximately 0.002 inch to the thickness of the band.

Instrumentation.- Pressure orifices and thermocouples were installed along the meridian lying in a vertical plane containing the center line of the model at distances from the cone apex as listed in figure 1. The diameter of the pressure orifices was 0.020 inch; transition to 0.070-inch i.d. tubing was made as close to the model surface as feasible. The orifices were connected to three groups of pressure transducers by way of three pressure scanning valves. A reference pressure was connected to one of the scanning-valve positions and used as a check on the calibration of the transducers. All thermocouples were iron constantan with the junction flush with the model surface. The method of thermocouple installation is shown in the detailed sketch in figure 1(a).

Test Methods and Techniques

Pressure and temperature measurements.- All pressure and temperature data of this investigation were recorded on magnetic tape and processed by an electronic data processing system. Tunnel stagnation pressure and temperature and boundary-layer impact pressures were also monitored visually on strip recorders and bourdon-type pressure gages. All pressure and temperature data presented were obtained at equilibrium wall temperatures. The repeatability of the wall static pressure ratio $p_w/p_{t,0}$ was within ±0.0001 on the conical forebody and within ±0.0004 at the rear of the compression surface. It is believed that the accuracy of the measured wall pressures corresponded to wall static pressure ratios of about one-half of the aforementioned $p_w/p_{t,0}$ values. The accuracy of the boundary-layer probe pressures is thought to have been within ±1 percent and the temperature measurements with ±2° R.

Boundary-layer surveys.- Boundary-layer surveys were made at two locations on both models - at $x = 10.55$ inches and $x = 19.87$ inches on the $\sigma = 10^\circ$

model, and at $x = 7.95$ inches and $x = 11.60$ inches on the $\sigma = 20^\circ$ model. A sketch of one of the flattened-tip total-pressure probes used in these surveys is presented in figure 3. A total of four probes were used to cover the range of surface inclination angles at the survey locations. The probe in use was connected directly to a group of three transducers covering ranges of 0 to 25, 50, and 100 psia. The low-range transducer was not used for the rearmost boundary-layer surveys. Probe contact with the surface of the model was indicated by a light when the probe touched a small, inlaid metal plate at the boundary-layer survey station. This position was taken as the wall position and all subsequent probe displacements were determined relative to the indicator reading for the wall position within an accuracy of ±0.0005 inch. After each movement of the probe during a boundary-layer survey the pressure indication from the probe was allowed to stabilize before data for that position were recorded.

RESULTS AND DISCUSSION

Model Surface Pressures

Static pressures obtained along the surfaces of the two center-body models are presented in figure 4 as a ratio of wall static pressure to tunnel stagnation pressure. The calculated pressure distribution for the sharp-nosed configuration of each model is also presented in this figure. The arrow labeled "End of cone" denotes the end of the conical forebody and the beginning of the isentropic compression surface.

The effect of nose radius on the wall pressures of the two models is small for both models. Except for the nose and shoulder regions, the difference in wall pressure between two configurations is generally within the repeatability of the data. The decrease in pressure noted at the front of the $\sigma = 20^\circ$ model (fig. 4(b)) is similar to that noted in reference 8 for a blunted-cone model at Mach 6.85. The measured pressures on the $r_n = 0$ configurations of both models are in good agreement with the calculated pressures except along the rear part of the isentropic compression surface. The measured pressures in this region are less than the predicted pressures by about 10 to 15 percent. The data show that wall pressures generally continue to increase on the short conical section following the isentropic compression surface.

Pressure distributions were also obtained for all configurations with boundary-layer trips and a typical example for each model is presented in figure 5. It will be noted that little or no difference in pressure occurred on the conical forebody for the range of trip sizes investigated. (The high pressures noted at $x = 2.1$ in. for three configurations of the $\sigma = 20^\circ$ model in fig. 5(b) are believed to have been caused by blockage of this orifice by the adhesive used to hold the roughness mounting band in place.) In general, there was some decrease in surface pressures on the rear part of the $\sigma = 10^\circ$ model as the boundary-layer trip size increased.

Mach number distributions obtained from the data of figure 4 and a calculated total pressure behind the bow shock are presented in figure 6 for the sharp-nosed configurations of both models. The Mach number distribution obtained from theoretical wall pressures is also presented for each model in figure 6 for comparison purposes. The total-pressure ratios used in the calculation of M_w from the pressure data were $p_{t,1}/p_{t,0} = 0.932$ for the $\sigma = 10^{\circ}$ model and $p_{t,1}/p_{t,0} = 0.521$ for the $\sigma = 20^{\circ}$ model. The flagged and filled symbols in this figure at the boundary-layer survey stations indicate the Mach number at the edge of the boundary layer as computed from measured and calculated pressures in the manner shown. (Data from the boundary-layer surveys are presented in a later section.) Except at the rearward survey station on the $\sigma = 10^{\circ}$ model, fairly good agreement is shown between the Mach number values obtained. The difference between the flagged and filled symbols at the rearward survey station on the $\sigma = 10^{\circ}$ model represents about an 8-percent difference in static pressure between the edge of the boundary layer and model surface.

Boundary-Layer Transition

Method of determining transition location.- The location of boundary-layer transition for the various configurations investigated was determined from model surface temperature distributions. This method (thermal) is one of several available for determining the location of transition, and makes use of the greater value of recovery temperature for turbulent flow relative to that for laminar flow. Since transition occurs over a distance equal to many boundary-layer thicknesses, the use of the term "transition point" is ambiguous unless a specific point in the transition region is specified. Therefore, for the remainder of this report, transition point (or location) will be taken to mean that point at which the boundary layer first becomes fully turbulent. This point was taken to coincide with the location of the maximum point in the surface temperature distributions. (See fig. 7.) Comparison of the transition point obtained by this method (thermal) with that determined from schlieren photographs (optical method) showed good agreement when the transition point in the photographs was assumed to occur where the boundary layer thickened and its edge began to have a feathery appearance. This point in the boundary layer is indicated by an arrow in the schlieren photographs of figure 8 for three of the several configurations investigated and was generally found to be 0.1 to 0.2 inch upstream of the point determined from the temperature distributions. Unfortunately, the change in wall temperature for some configurations occurred in a region on the model where the spacing between thermocouples was relatively large. Consequently, the determination of the location of transition in this region is a matter of judgment in fairing a curve through the data points. Transition occurred in this region for the blunt-nosed configurations, and since these configurations produced a shear layer that tended to mask the boundary layer (unless the sensitivity of the schlieren apparatus was carefully adjusted) verification of the transition point by the schlieren photographs was not possible for all configurations.

Effect of nose bluntness on transition.- Model-surface temperature distributions showing the effect of nose blunting on transition location are presented in figure 9 for the two center-body models. These distributions are for equilibrium surface temperatures, although it was found that the transition point was affected very little by surface temperatures less than equilibrium values. The ratio of adiabatic-wall or recovery temperature to stagnation temperature for the conical forebody only is indicated on figure 9 for laminar and turbulent flow. These ratios were computed by assuming a recovery factor of 0.85 for laminar flow and 0.90 for turbulent flow and by using the inviscid sharp-nose-cone surface Mach number.

The data of figure 9 show that blunting the nose of the center body increases the distance to transition by about 50 percent or more when compared with the transition location of the sharp-nosed configuration. This increase to transition occurs for both models for the smallest value of nose radius $\left(r_n = 0.14 \text{ in.}\right)$ and, as seen in the following table, does not change by a great amount with nose radii greater than 0.14 inch.

$\sigma = 10^\circ$					$\sigma = 20^\circ$				
r_n, in.	x_{tr}, in.	x'_{tr}, in.	s_{tr}, in.	s_{tr}/r_n	r_n, in.	x_{tr}, in.	x'_{tr}, in.	s_{tr}, in.	s_{tr}/r_n
0	9.1	9.1	9.2	-----	0	5.6	5.6	5.9	----
.14	14.8	14.1	14.4	102.9	.14	9.9	9.6	10.4	74.0
.28	15.5	14.2	14.5	51.9	.28	10.0	9.5	10.3	36.8
.45	17.0	14.9	15.4	34.1	.45	10.2	9.3	10.2	22.6

The small differences in the transition distance noted between the blunt-nosed configurations are not considered to be of any significance as these distances can be increased or decreased slightly by refairing the curves through the data points.

The values of s_{tr} listed in the preceding table were used in determining a transition Reynolds number for the various configurations. These data are presented in figure 10 as a function of bluntness Reynolds number which is based on tunnel test-section conditions and the diameter of the center-body nose. The transition Reynolds numbers shown are approximate values since boundary-layer surveys were not made at the transition locations. These values were obtained by using the shape of the inviscid sharp-nose Reynolds number distribution curve to fair a curve through the data points obtained for all configurations at the two boundary-layer survey stations. This procedure was considered to be valid since transition occurred close to or between the survey stations and the curve was essentially a straight line in this region. Figure 10 (at $R_b = 0$) shows that the transition Reynolds number for the sharp-nosed $\sigma = 10^\circ$ model is greater than that for the sharp-nosed $\sigma = 20^\circ$ model. This result agrees with previous experiments (refs. 2 and 3, for example) that show R_{tr} increasing with Mach number above a Mach number of about 3.4. Except for the $r_n = 0.28$ configuration of the $\sigma = 10^\circ$ model $\left(R_b = 3.17 \times 10^5\right)$ this trend is also noted for the blunt-nosed configurations. The increase in R_{tr} for the blunt-nosed configurations over the value for the sharp-nosed bodies noted in figure 10 cannot be directly compared with results from pure cones since transition for the blunt-nosed configurations occurs on the isentropic compression surface. Along this surface the Mach number decreases and the unit Reynolds number increases with distance from the nose. Both Mach number and unit Reynolds number can influence the transition Reynolds number and for the case of a cone or flat plate the effect of one parameter can cancel the effect of the other. (See ref. 3.) Coupled with these two parameters is the influence of increasing static pressure along the compression surface; this pressure may override the influence of boundary-layer outer-edge Mach number and unit Reynolds number on the distance to transition.

The schlieren photographs of figure 11 show the general flow pattern about the models. Transition occurred before the flow reached that region of the model where the pressure increases rapidly so that separation of the flow in this region did not occur.

Effect of controlled surface roughness on transition.- Although fixing the transition by artificial means was not necessary for the models of this investigation, it was felt that the small amount of data available on surface roughness effects at hypersonic speeds justified an extension of this investigation to explore these effects. Calculation of the critical roughness size (defined as the minimum size necessary to influence transition location) by the method of reference 9 showed that this size was much smaller than the spheres available at the time of these experiments. The sphere diameters for critical roughness for the sharp-nosed configurations were about 0.015 inch at $x = 5$ inches for the $\sigma = 10^{\circ}$ model and about 0.007 inch at $x = 2.5$ inches for the $\sigma = 20^{\circ}$ model, whereas the smallest sphere diameter available was 0.031 inch. (The critical-roughness Reynolds number used for this calculation was assumed to be 800.) According to reference 10, only a small increase in roughness or trip size over the critical value is required to move the location of transition upstream to essentially the trip location at the lower Mach numbers, that is, up to $M \approx 4$. At Mach numbers greater than 4, however, reference 10 states that fixing transition near the roughness location may become increasingly difficult and indicates that a roughness height considerably greater than the critical value (defined in ref. 9) may be required. Also, for the blunt-nosed configurations of the present investigation, an even greater trip height is required to fix transition because of the decreasing unit Reynolds number at the boundary-layer outer edge with increasing bluntness. (See ref. 11.) Accordingly, wall-temperature distributions were obtained for all configurations of both models with roughness spheres of 0.031, 0.047, and 0.063 inch in diameter. These distributions and the corresponding schlieren photographs are presented in figures 12 to 15. Included in figures 12 and 14 for the $r_n = 0$ and $r_n = 0.45$ inch configurations are distributions obtained with only the roughness mounting band in place.

Inspection of the data for the sharp-nosed $\sigma = 10^{\circ}$ model in figure 12(a) shows that transition occurs at or very near the trip location for the range of trip sizes investigated. Relative to the two larger trip sizes, however, there is a small delay in transition for $k = 0.031$ inch. Addition of the mounting band alone moved transition upstream about 1 inch. This increase in distance was unexpected in that the height of the band was much less than a calculated two-dimensional critical roughness size and therefore should not have affected the location of transition. The temperature distributions for the $r_n > 0$ configurations in figures 12(b) to 12(d) definitely show that transition was fixed close to the trip location for $k = 0.063$ inch. These figures do not clearly show whether transition occurred at the trip location for k values of 0.031 and 0.047 inch or somewhat further downstream. The temperature distributions for these roughness sizes show an initial peak value slightly downstream from the trip location and a second, but higher, peak temperature ratio further downstream. For the $\sigma = 20^{\circ}$ model at a cone surface Mach number of 3.75 (fig. 14), the temperature distributions leave little doubt that transition was fixed at the trip location for all combinations of trip size and nose configurations. The mounting band for the $r_n = 0$ configuration of this model (fig. 14(a)) had an effect opposite to that noted for the $\sigma = 10^{\circ}$ model (fig. 12(a)); that is, the location of transition was delayed by about 1 inch by the band on the $\sigma = 20^{\circ}$ model. For the $r_n = 0.45$ configurations the band had no effect on the location of transition.

A comprehensive investigation of controlled roughness effects on transition on a flat plate at hypersonic speeds is reported in reference 12 and the results presented herein on roughness effects will be discussed in the light of the results from this reference. In accord with reference 12, the critical roughness size will be redefined as the trip size necessary to move transition upstream to essentially the trip location. Calculation of a roughness Reynolds number was approximate for the present investigation, particularly so for the $r_n > 0$ configurations, since boundary-layer surveys were not made at the trip location; the roughness Reynolds number is based on the roughness height (sphere diameter in this case) and flow conditions at the boundary-layer outer edge. The unit Reynolds number at the trip location for the blunt-nosed configurations was obtained from measured wall pressures and from the Mach number at the boundary-layer outer edge computed by the method of reference 11. A summary of roughness Reynolds numbers obtained by this procedure for the $\sigma = 10^{\circ}$ model is presented in figure 16. Results for the $\sigma = 20^{\circ}$ model were not reduced to this form since transition on this model was fixed at the trip location for all trip sizes investigated. In figure 16 the roughness Reynolds numbers for the three roughness sizes and the four nose configurations are indicated by symbols and are plotted at the surface distances corresponding to the roughness location on the model. Since this location was at a fixed distance from the apex of the conical forebody, the surface distance to this point decreased as the nose radius increased. The arrows below the abscissa indicate the location of transition as determined from the temperature distributions for the four nose configurations. The transition location was chosen to correspond with the maximum peak temperature ratio and not the initial peak value. The data in figure 16 indicate that a critical roughness Reynolds number of about 32,400 $\left(\sqrt{R_k} = 180\right)$ is required to fix transition at the trip location. That is, the transition is located at the trip location for values of $\sqrt{R_k}$ greater than 180 and somewhat downstream for values less than 180. With the assumption that the unit Reynolds numbers at the boundary-layer outer edge and at the top of the roughness are essentially equal, the $\sqrt{R_k}$ values of this investigation may be compared directly with the critical roughness Reynolds number values of reference 12. This comparison shows that $\sqrt{R_k} = 180$ lies about midway in the range of values observed in this reference for a flat plate. The Reynolds number at the trip location $\left(1.35 \times 10^{6} \text{ to } 3.80 \times 10^{6}\right)$ for this investigation included the range of reference 12, and the boundary-layer outer-edge Mach numbers were essentially the same ($M_\delta \approx 5$). As a matter of interest, the minimum value of $\sqrt{R_k}$ investigated for the $\sigma = 20^\circ$ model was about 200. The original concept of a constant value of critical roughness Reynolds number (as defined in ref. 9) applied only to roughness submerged in the boundary layer. In the present investigation and in reference 12, the critical roughness size was found to be greater than the boundary-layer thickness by about a factor of 2. Thus, in these cases the critical roughness Reynolds number can no longer be constant but varies with flow conditions external to the boundary layer.

Boundary-Layer Surveys

Results from the total-pressure surveys made of the boundary layer on the models of this investigation are presented and discussed in this section. As noted previously, the boundary-layer-survey locations were near the end of the conical forebody and isentropic compression surface on both models. Velocity ratios through the boundary layer were computed from the survey data by assuming that the static pressure and total temperature through the boundary layer were constant and respectively equal to the wall pressure at the survey station and the tunnel stagnation temperature. These velocity ratios and the corresponding values of displacement and momentum thicknesses are presented in figures 17 to 22 for the two models without roughness and in figures 23 to 26 for the sharp-nosed models with roughness.

The assumption of constant static pressure through the boundary layer is felt to be valid at the forward survey station because of the essentially zero pressure gradient along the surface and because of the thinness of the boundary layer. Although the boundary layer at the rearward survey station was also thin and although a large static pressure gradient through the boundary layer is improbable, the data (δ^* and θ, in particular) are questionable in view of the rapidly changing flow conditions with distance in this region. Experimental data in reference 13 show that the effect on the velocity profile of assuming a constant total temperature through the boundary layer is small for a cone having nearly adiabatic-wall temperatures.

The boundary-layer thickness, and therefore the velocity at the edge of the boundary layer, was chosen from the experimental data by inspection of plots of $p_{t,2}$ as a function of y_s. This procedure was straightforward for the sharp-nosed configurations but was compromised somewhat for the $r_n > 0$ configurations by the shear layer external to the boundary layer; that is, the velocity gradient in the external shear layer tended to mask the edge of the boundary layer in the pitot pressure profiles, thus the procedure of reference 5 was used to determine δ for these profiles. In this reference a small inflection was noted in the profiles at the edge of the boundary layer. An inflection point was also observed in the profiles for some of the $r_n > 0$ configurations of the present investigation. Therefore, this point was taken as the edge of the boundary layer when a clear-cut location was lacking in the pitot pressure data.

Effect of nose bluntness on boundary-layer parameters.- The velocity profiles for the $\sigma = 10^{\circ}$ model in figure 17(a) show a decrease in boundary-layer thickness δ at the foward survey station (x = 10.55 in.). This decrease was due to the change from turbulent to laminar flow at this point as the nose radius increased from 0 to 0.14 inch. (See fig. 9(a).) Increasing the nose radius further causes δ to increase. This same trend of the data is noted at the rearward survey station (fig. 17(b)), although the change in boundary-layer thickness with nose radius is smaller at this station. The calculation of the boundary-layer outer-edge Mach number for the roughness data in the previous section showed that this Mach number reached the inviscid sharp-nosed cone value upstream of the forward survey station for the three nose radii investigated. However, the experimental data of figure 17(a) show that M_{δ} decreased at the forward survey station as the nose radius increased. At the rearward survey station there was essentially no change in M_{δ} between the blunt-nosed configurations although M_{δ} had decreased from the sharp-nose value.

The velocity profiles of figure 17 are presented in figure 18 with the distance from the model surface nondimensionalized with respect to the displacement thickness. Presented in this figure are the values of momentum and displacement thicknesses and the boundary-layer outer-edge Reynolds number based on the momentum thickness. It will be noted that the location of transition on the sharp-nosed configuration is about an inch upstream of the forward survey station. Thus, the value of momentum thickness Reynolds number given in figure 18 for $r_n = 0$ is close to the value at transition. Momentum and displacement values presented in figure 18 are plotted in figure 19 as a function of the nose radius. It is seen in this figure that both the momentum and displacement thicknesses increase with nose radius at the forward station. At the rearward survey station these parameters show the greatest change from the sharp-nose values at $r_n = 0.45$ inch.

Results from the surveys on the $\sigma = 20^{\circ}$ model are presented in figures 20 to 22 in the same manner as the $\sigma = 10^{\circ}$ data. Differences will be noted in the general trend of the data between the two models in these figures. The boundary-layer thickness showed a continuing increase with nose radius at the forward survey station and a small decrease with increasing nose radius at the rearward station. The boundary-layer outer-edge Mach number at the forward station increased above the value for the sharp-nosed cone $\left(M_{\delta} = 3.78\right)$ with nose blunting for the $\sigma = 20^{\circ}$ model and was essentially unchanged at the rearward station. At the rearward survey station, nose radius had very little effect on displacement or momentum thickness except for the $r_n = 0.14$ configuration. The abrupt increase in these parameters for this configuration suggests a data error as it is not reasonable to expect the smallest nose radius to have the greatest effect on the boundary layer. Since the source of the error was not obvious, the curve was faired through the data point obtained.

Effect of roughness on boundary-layer parameters.- The effect of roughness on the velocity profiles of the two models will be noted in the nondimensional profiles of figures 23 and 25. The boundary-layer thickness shows a general increase with roughness except at the rearward survey station on the $\sigma = 20^{\circ}$

model where a small decrease in δ occurred. This result may be associated with the assumption of constant static pressure through the boundary layer in this region of the model and with the shock from the roughness particles. Although it is barely discernible in the schlieren photographs of figure 15, the bow shock from the roughness particles is reflected from the model bow shock toward the shoulder region of the model. The photographs do not clearly show whether this reflected shock strikes the surface before the rearward survey station or behind it. The velocity deficiency noted in the profiles of figure 25(b) for $k > 0$ suggests that the reflected shock impinges on the surface close to the survey station and thus disturbs the flow in this region.

The effect of roughness on momentum and displacement thicknesses at the forward survey station was somewhat erratic (figs. 24 and 26). The rather large increase in δ^* and θ at this survey station on the $\sigma = 20^\circ$ model for $k = 0.031$ inch is a result of a velocity deficiency close to the surface of the model. (See fig. 25(a).) A similar, but smaller, deficiency is seen for this roughness size on the $\sigma = 10^\circ$ model in figure 23(a). If the results for this roughness size are ignored in figure 26, then the effect of off-design roughness sizes on δ^* and θ would be small for the $\sigma = 20^\circ$ model. Similarly, for the $\sigma = 10^\circ$ model in figure 24, δ^* and θ would increase at the forward survey station as the roughness size increases. At the rearward survey station on this model, the remaining data point for $k = 0.063$ inch would suggest that these parameters decrease with increasing roughness size.

SUMMARY OF RESULTS

Results from an investigation of nose blunting and controlled roughness effects on the pressure recovery, location of transition, and boundary-layer parameters of two center bodies from an all-external-compression hypersonic inlet at a free-stream Mach number of 5.98 are summarized.

1. Nose blunting effects on surface pressures were restricted essentially to the initial portion of the conical forebody.

2. Natural transition to turbulent flow on the sharp-nosed configurations was found to be in agreement with the trend of increasing transition Reynolds number with increasing Mach number noted in previous investigations for flat plates and cones at Mach numbers above 3.4.

3. Transition to turbulent flow was delayed with nose blunting. In addition, the transition Reynolds number for the blunt-nosed configurations was found to be larger than the transition Reynolds number for the sharp-nosed configurations. Transition location and transition Reynolds number were essentially unaffected by nose radii greater than 0.14 inch.

4. Investigation of the effects of controlled roughness on transition showed that for the 10° forebody at a surface Mach number of about 5 the roughness size necessary to fix transition at the roughness location exceeded the height of the boundary layer at this location by a factor of about 2. This

result was in agreement with recent data (NASA TN D-2054) obtained on a flat plate at Mach numbers of 4.8 and 6.0.

5. Roughness was found to have little effect on surface pressures even for roughness sizes several times larger than that required to fix transition.

6. Boundary-layer momentum and displacement thicknesses generally increased with increasing nose radius. Roughness size effects on these parameters varied with the model and survey location. Both roughness and nose blunting effects on the momentum and displacement thicknesses tended to be attenuated as the flow progressed toward the rear of the model.

Langley Research Center,
National Aeronautics and Space Administration,
Langley Station, Hampton, Va., March 22, 1965.

REFERENCES

1. Moeckel, W. E.: Some Effects of Bluntness on Boundary-Layer Transition and Heat Transfer at Supersonic Speeds. NACA Rept. 1312, 1957. (Supersedes NACA TN 3653.)

2. Laufer, John; and Marte, Jack E.: Results and a Critical Discussion of Transition-Reynolds-Number Measurements on Insulated Cones and Flat Plates in Supersonic Wind Tunnels. Rept. No. 20-96 (Contract No. DA-04-495-Ord 18), Jet Propulsion Lab., Nov. 30, 1955.

3. Brinich, Paul F.; and Sands, Norman: Effect of Bluntness on Transition for a Cone and a Hollow Cylinder at Mach 3.1. NACA TN 3979, 1957.

4. Van Driest, E. R.; and McCauley, W. D.: The Effect of Controlled Three-Dimensional Roughness on Boundary-Layer Transition at Supersonic Speeds. J. Aero/Space Sci., vol. 27, no. 4, Apr. 1960, pp. 261-271, 303.

5. Rogers, Ruth H.: Boundary Layer Development in Supersonic Shear Flow. AGARD Rept. 269, Apr. 1960.

6. Potter, J. Leith; and Whitfield, Jack D.: Effects of Unit Reynolds Number, Nose Bluntness, and Roughness on Boundary Layer Transition. AGARD Report 256, Apr. 1960.

7. Sterrett, James R.; and Emery, James C.: Extension of Boundary-Layer-Separation Criteria to a Mach Number of 6.5 by Utilizing Flat Plates With Forward-Facing Steps. NASA TN D-618, 1960.

8. Bertram, Mitchel H.: Tip-Bluntness Effects on Cone Pressures at $M = 6.85$. J. Aeron. Sci. (Readers' Forum), vol. 23, no. 9, Sept. 1956, pp. 898-900.

9. Braslow, Albert L.; and Knox, Eugene C.: Simplified Method for Determination of Critical Height of Distributed Roughness Particles for Boundary-Layer Transition at Mach Numbers From 0 to 5. NACA TN 4363, 1958.

10. Braslow, Albert L.: Review of the Effect of Distributed Surface Roughness on Boundary-Layer Transition. AGARD Rept. 254, Apr. 1960.

11. Rubin, Irving: Shock Curvature Effect on the Outer Edge Conditions of a Laminar Boundary Layer. AIAA J., vol. 1, no. 12, Dec. 1963, pp. 2850-2852.

12. Holloway, Paul F.; and Sterrett, James R.: Effect of Controlled Surface Roughness on Boundary-Layer Transition and Heat Transfer at Mach Numbers of 4.8 and 6.0. NASA TN D-2054, 1964.

13. Bradfield, Walter S.: An Experimental Investigation of the Turbulent Boundary Layer in Supersonic Flow Around Unyawed Cones With Small Heat Transfer and Correlations With Two Dimensional Data. Res. Rept. No. 1, Convair Sci. Res. Lab., Mar. 15, 1958.

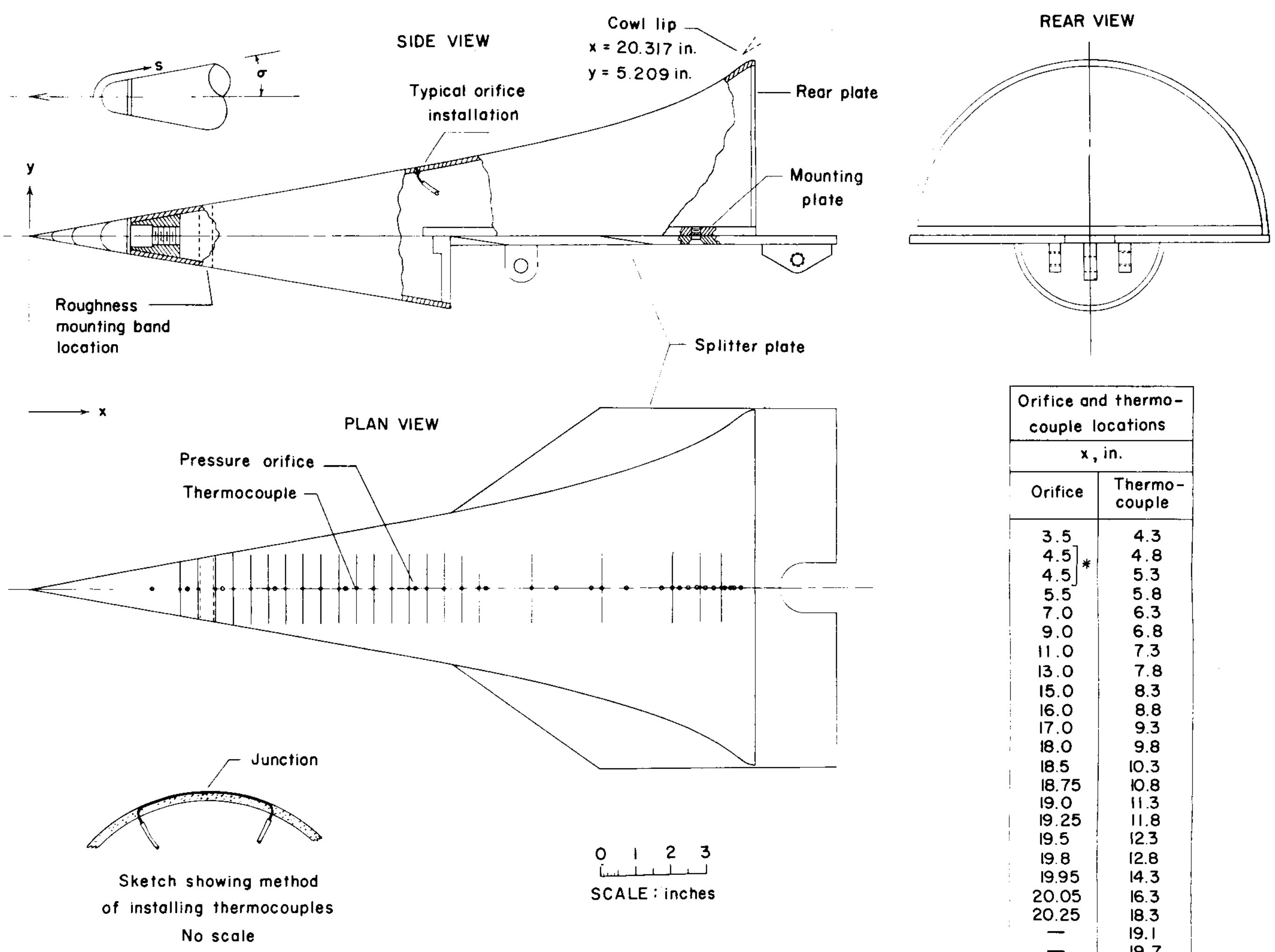

Surface coordinates	
x, in.	y, in.
10.710	1.888
10.8	1.903
11.3	1.993
11.8	2.088
12.3	2.184
12.8	2.283
13.3	2.387
13.8	2.496
14.3	2.610
14.8	2.729
15.3	2.853
15.8	2.985
16.3	3.124
16.8	3.273
17.3	3.433
17.8	3.607
18.3	3.797
18.8	4.003
19.05	4.119
19.3	4.248
19.55	4.388
19.7	4.482
19.8	4.550
19.85	4.579
Conical surface	
20.304	4.900
20.4	4.958
20.5	4.998
20.6	5.021
20.7	5.030

Orifice and thermocouple locations	
x, in.	
Orifice	Thermocouple
3.5	4.3
4.5*	4.8
4.5*	5.3
5.5	5.8
7.0	6.3
9.0	6.8
11.0	7.3
13.0	7.8
15.0	8.3
16.0	8.8
17.0	9.3
18.0	9.8
18.5	10.3
18.75	10.8
19.0	11.3
19.25	11.8
19.5	12.3
19.8	12.8
19.95	14.3
20.05	16.3
20.25	18.3
—	19.1
—	19.7

* 180° apart

(a) $\sigma = 10^\circ$.

Figure 1.- Models.

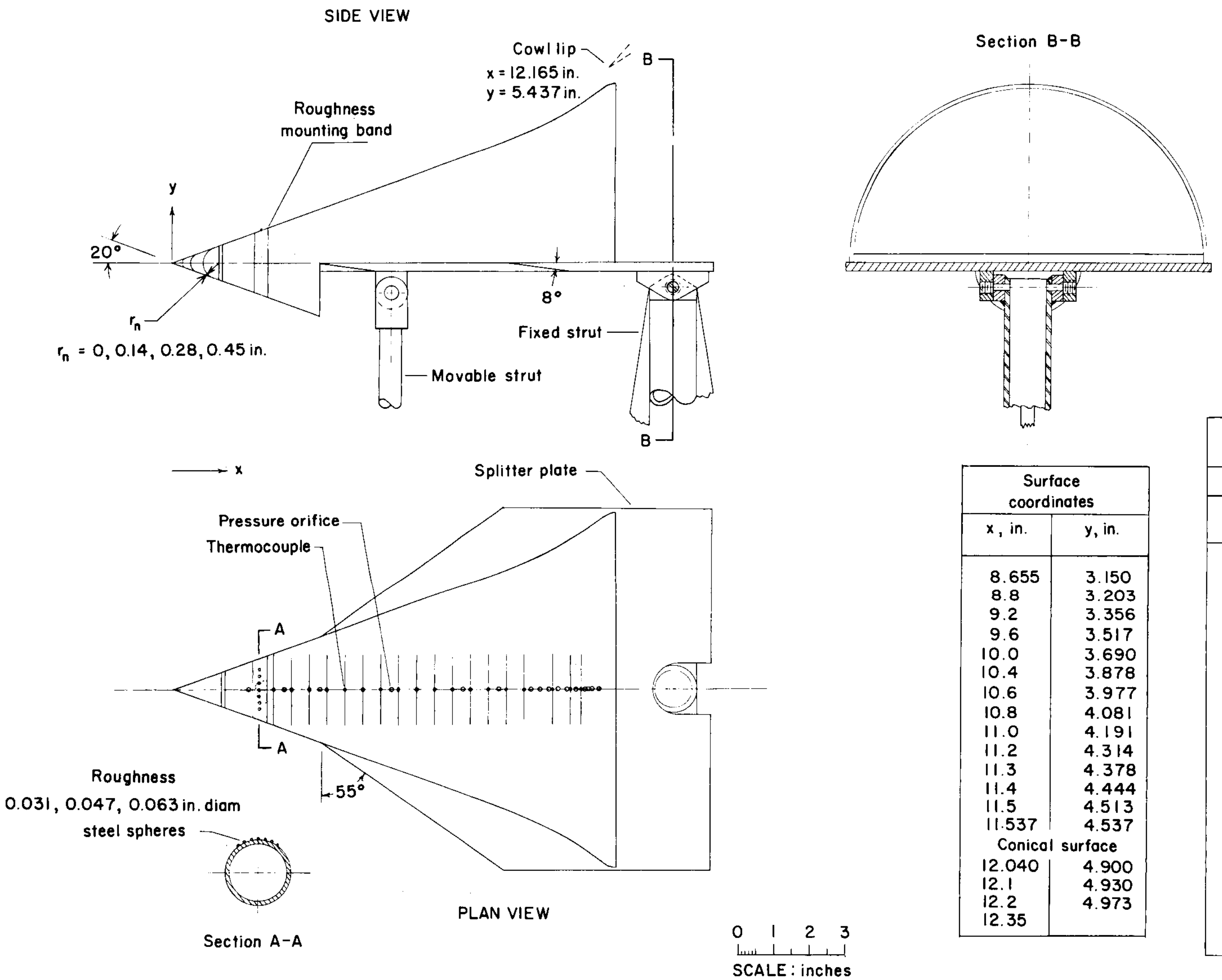

Surface coordinates	
x, in.	y, in.
8.655	3.150
8.8	3.203
9.2	3.356
9.6	3.517
10.0	3.690
10.4	3.878
10.6	3.977
10.8	4.081
11.0	4.191
11.2	4.314
11.3	4.378
11.4	4.444
11.5	4.513
11.537	4.537
Conical surface	
12.040	4.900
12.1	4.930
12.2	4.973
12.35	

Orifice and thermocouple locations	
x, in.	
Orifice	Thermocouple
2.1	3.3
3.1 *	2.8
3.1 *	3.3
3.1	3.8
4.1	4.3
6.1	4.8
8.1	5.3
9.1	5.8
10.0	6.3
10.25	6.8
10.5	7.3
10.75	7.8
11.00	8.3
11.25	8.8
11.50	9.3
11.6	9.8
11.7	10.6
11.9	11.1
—	11.4

* 180° apart

(b) $\sigma = 20^{\circ}$.

Figure 1.- Concluded.

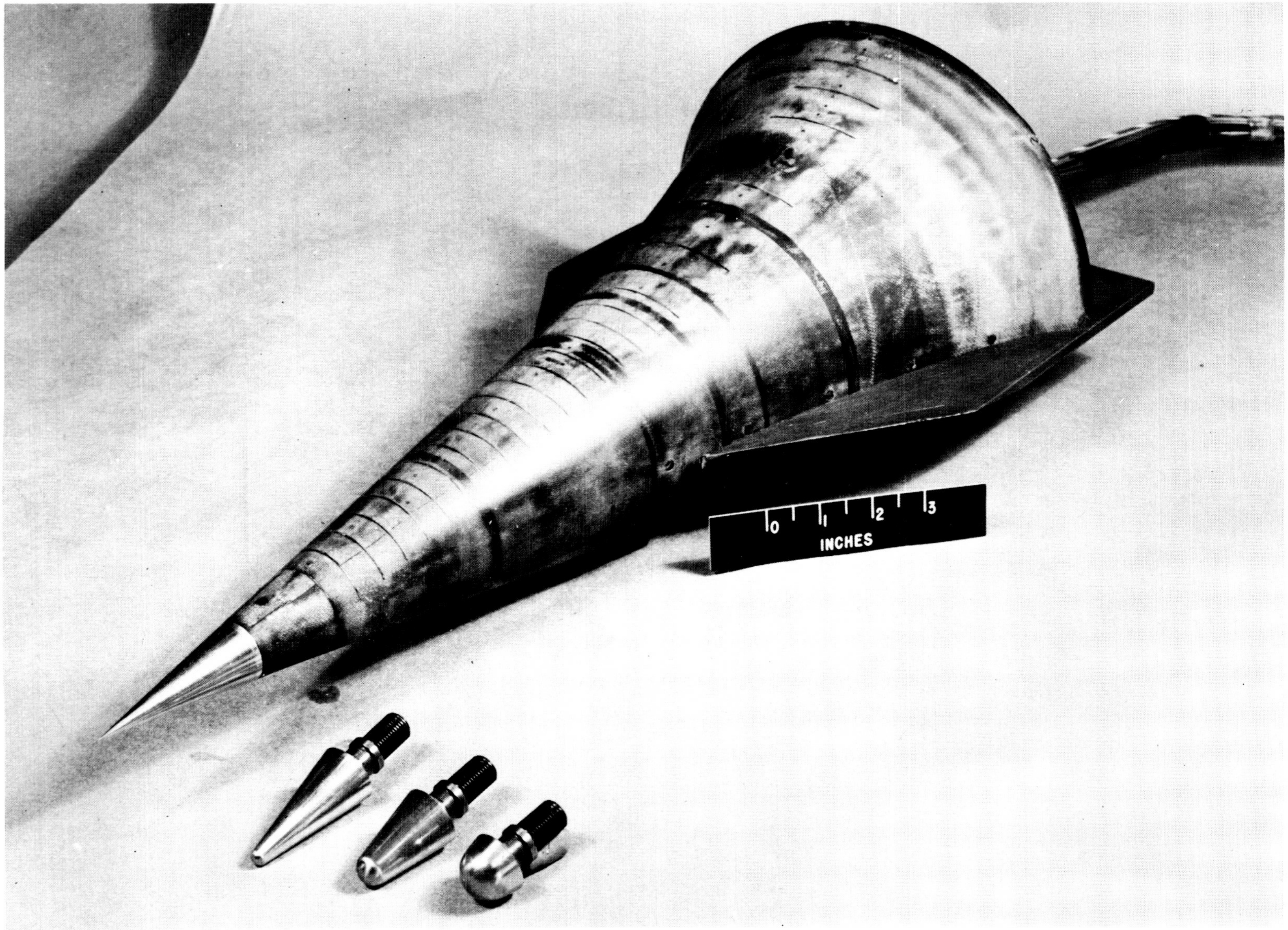

(a) σ = 10°.

L-64-4340

Figure 2.- Photographs of models.

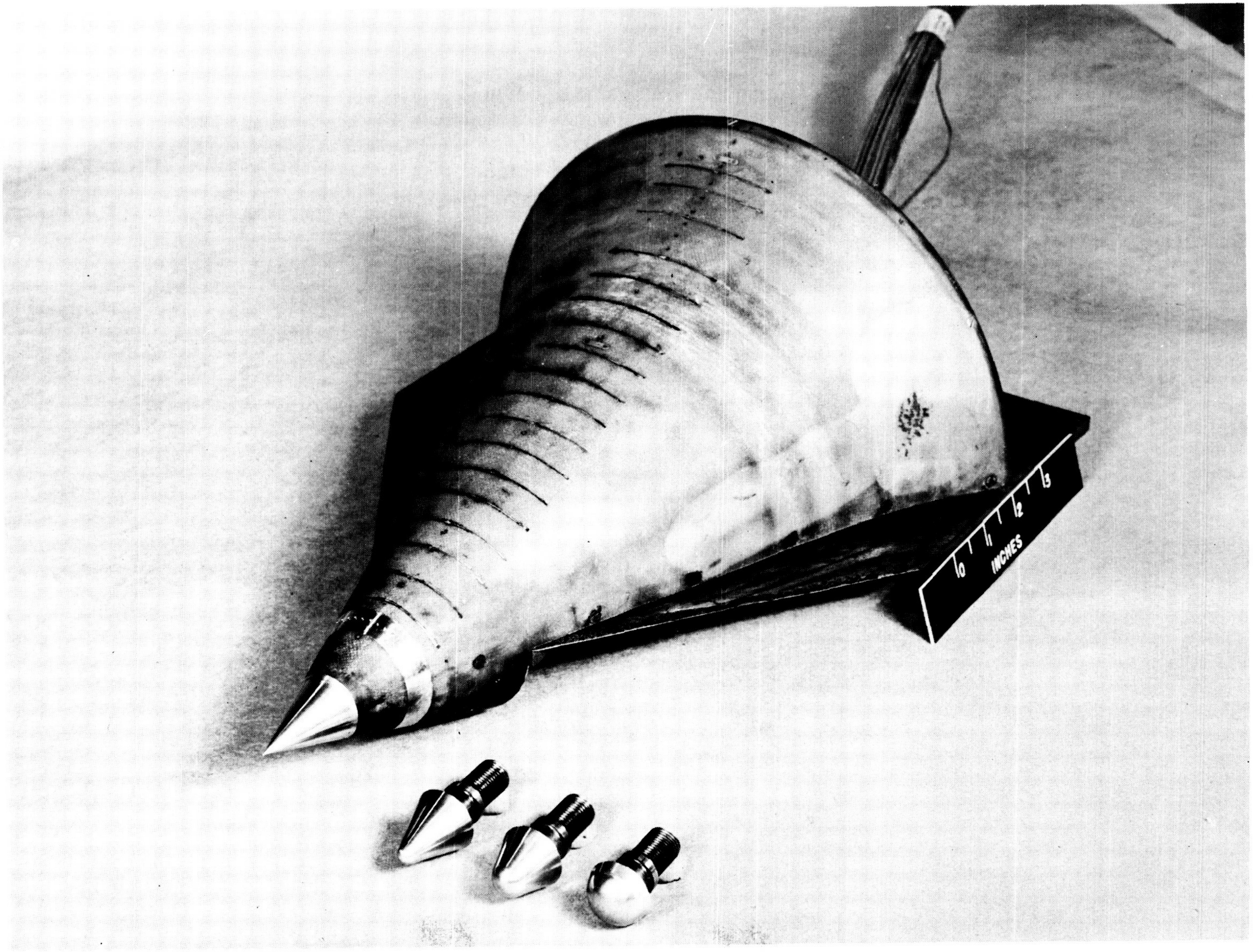

(b) $\sigma = 20^{\circ}$.

L-64-4339

Figure 2.- Continued.

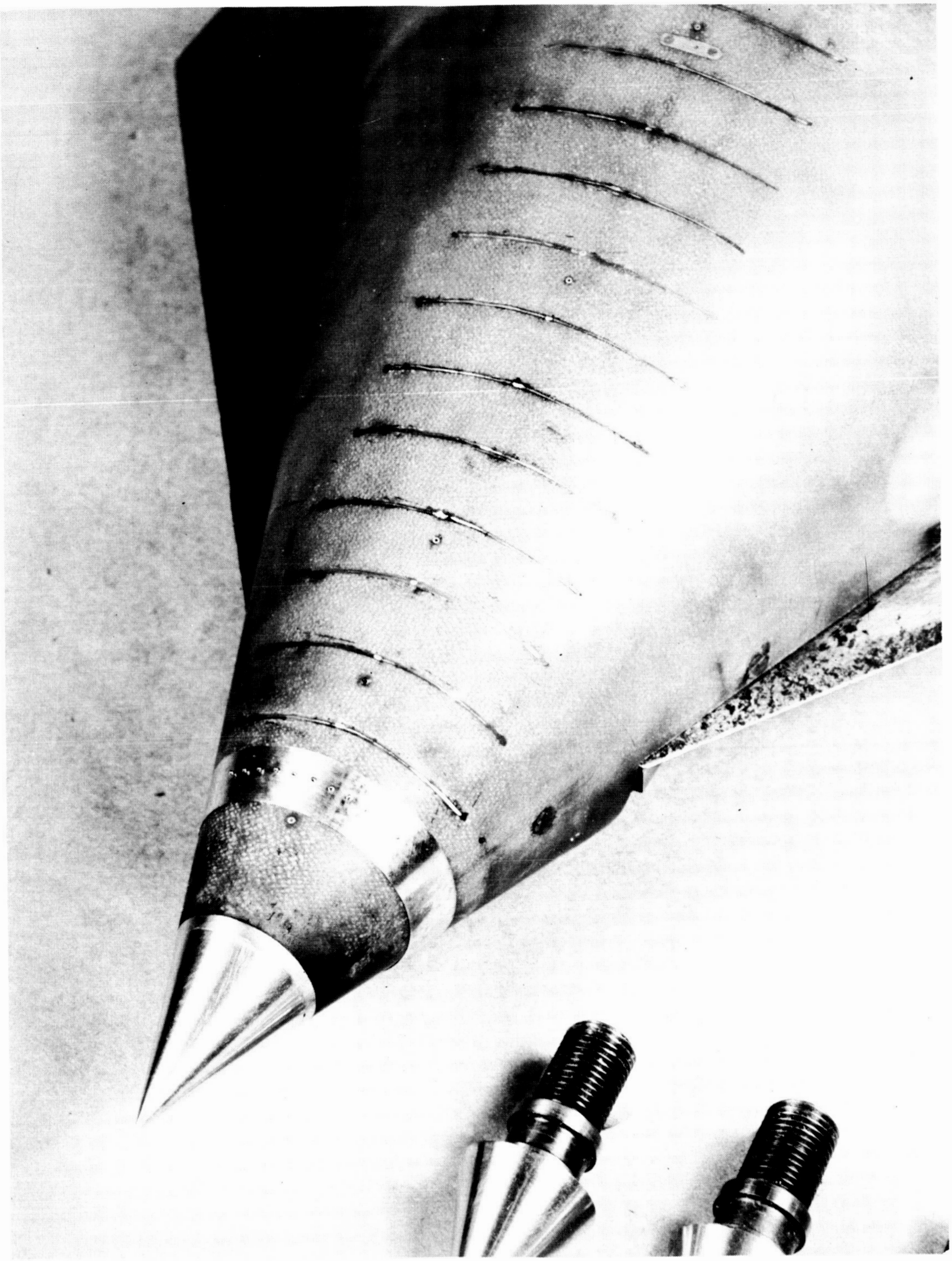

(c) Close-up of trip mounting band and trip; k = 0.031 in. L-64-4341

Figure 2.- Concluded.

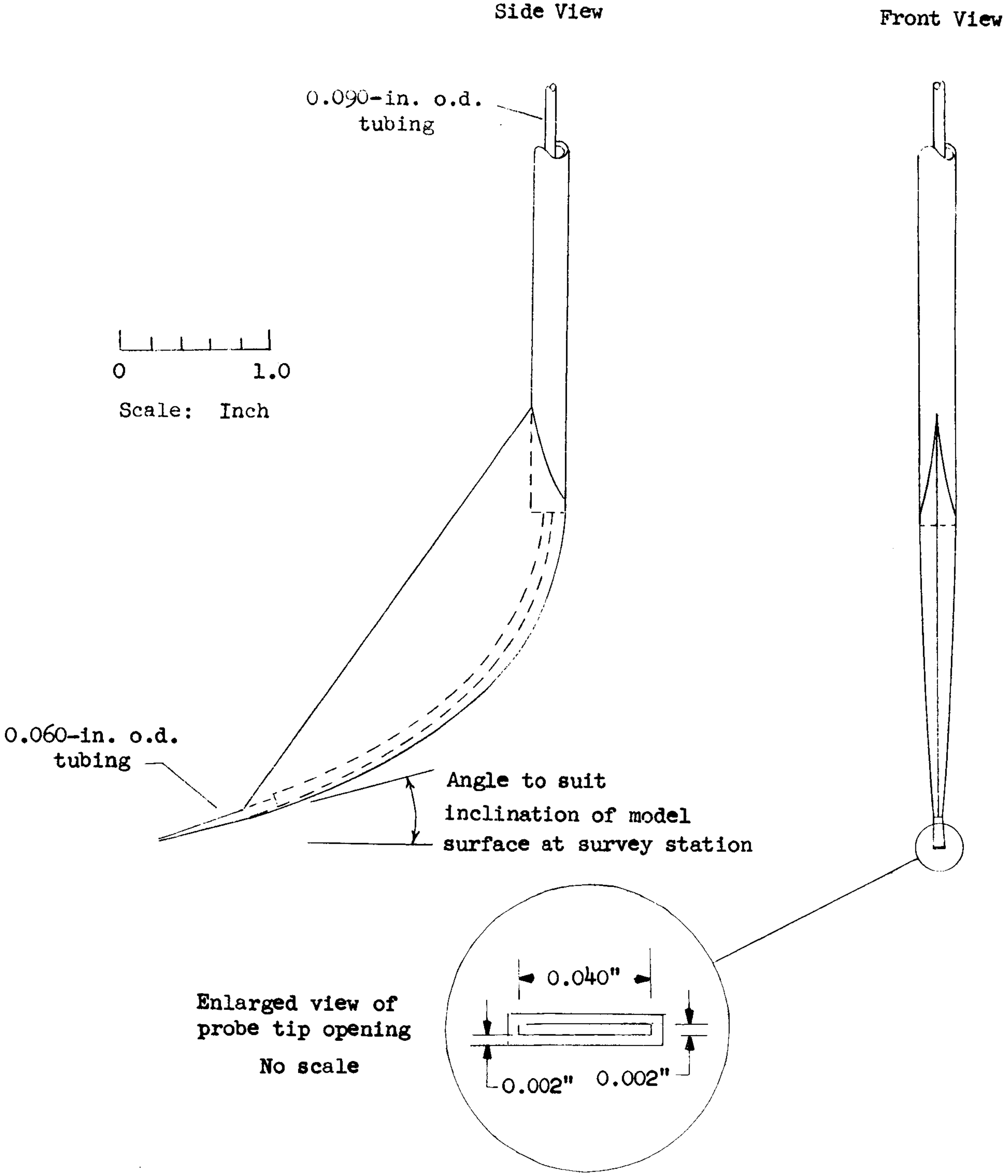

Figure 3.- Typical boundary-layer survey probe.

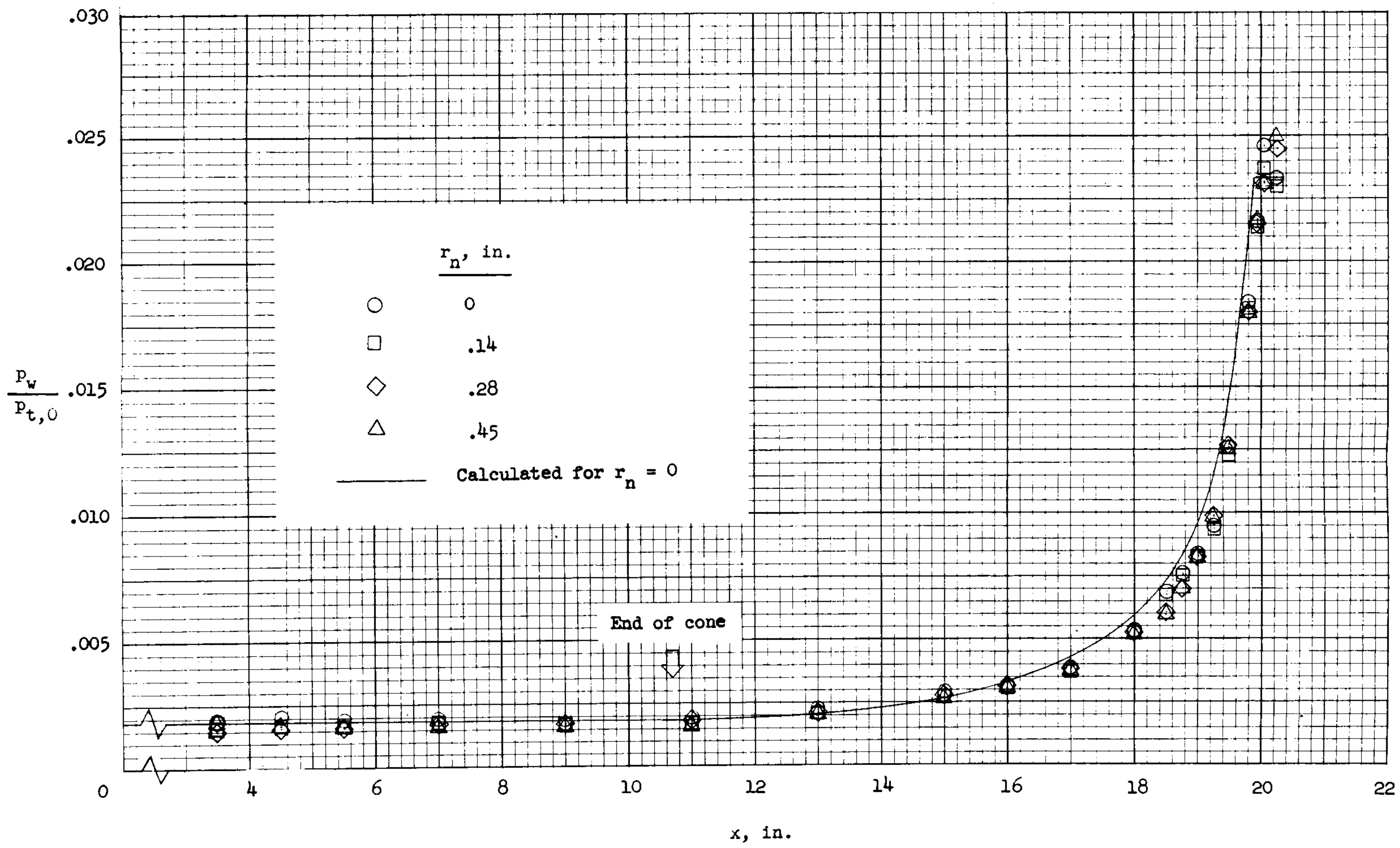

(a) $\sigma = 10^{\circ}$.

Figure 4.- Effect of nose radius on surface pressures.

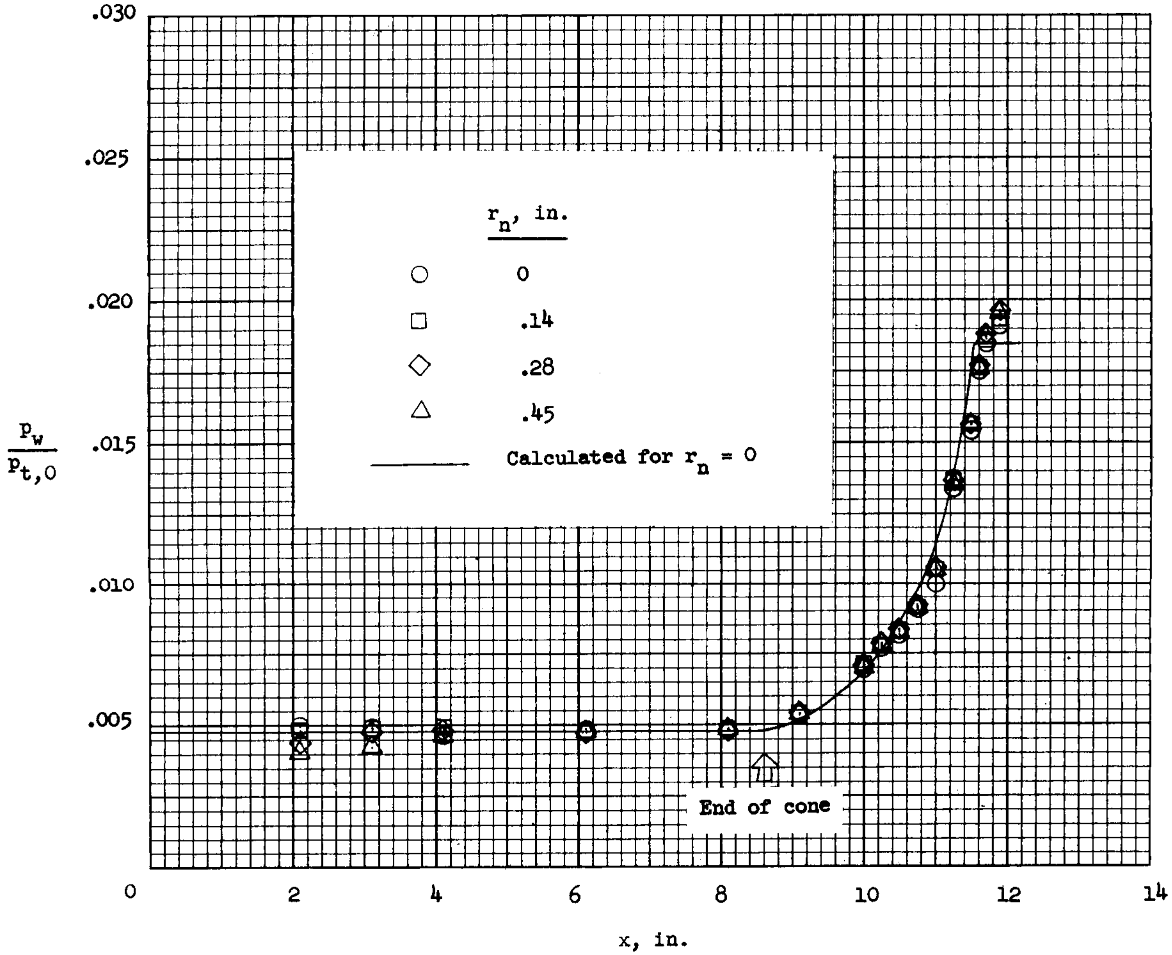

(b) $\sigma = 20^\circ$.

Figure 4.- Concluded.

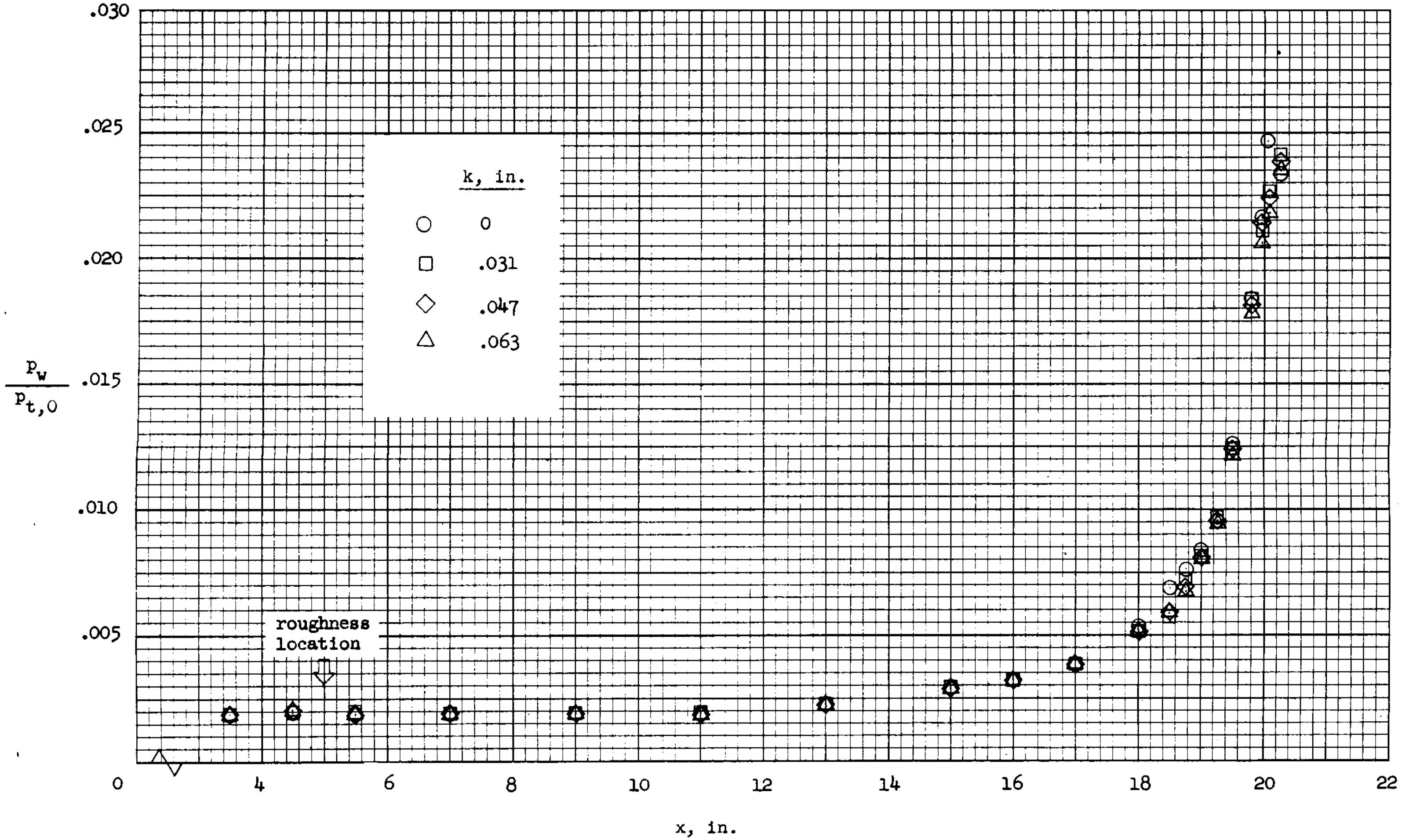

(a) $\sigma = 10^{\circ}$.

Figure 5.- Effect of boundary-layer trip size on surface pressures; $r_n = 0$.

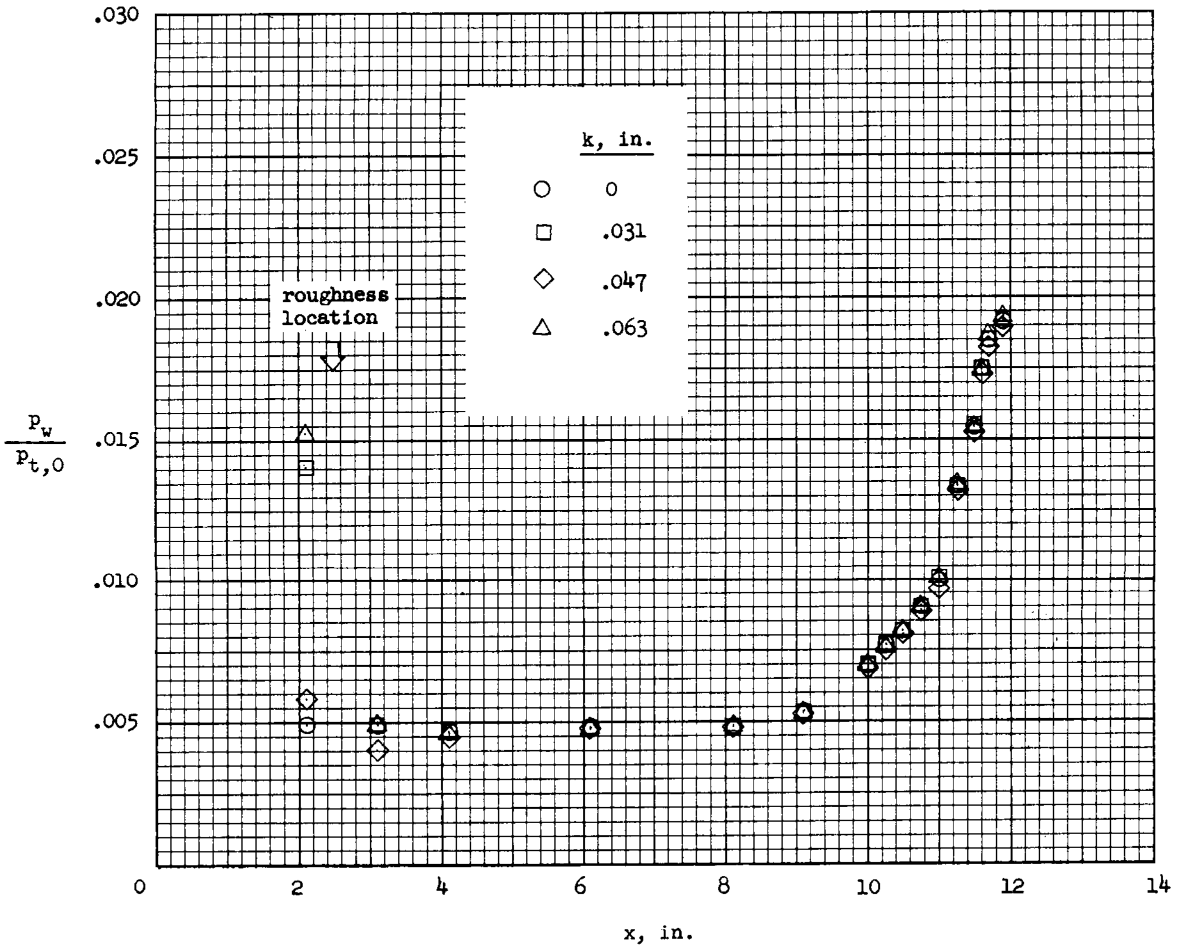

(b) $\sigma = 20^{\circ}$.

Figure 5.- Concluded.

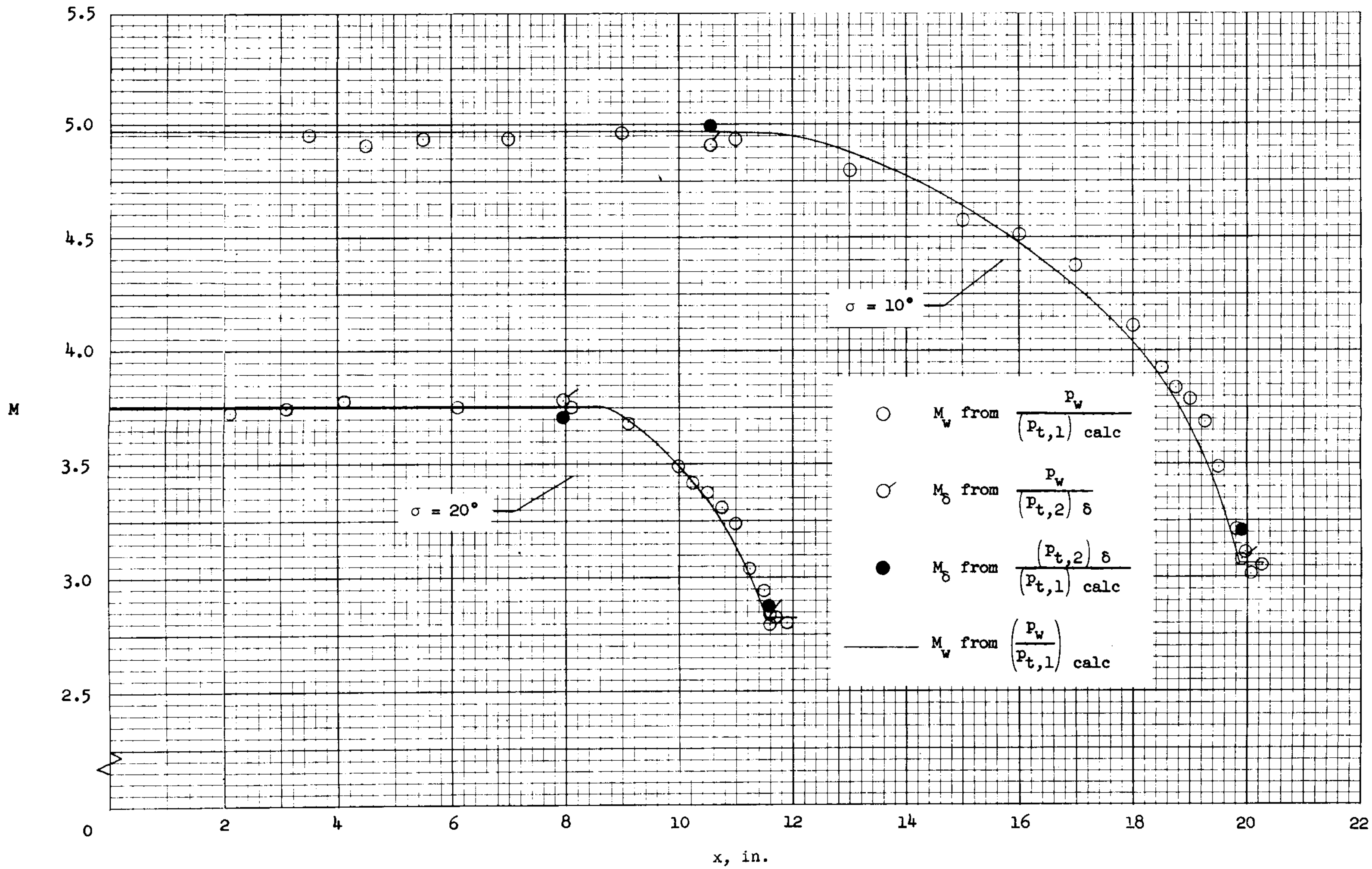

Figure 6.- Mach number distribution along model surface; $r_n = 0$.

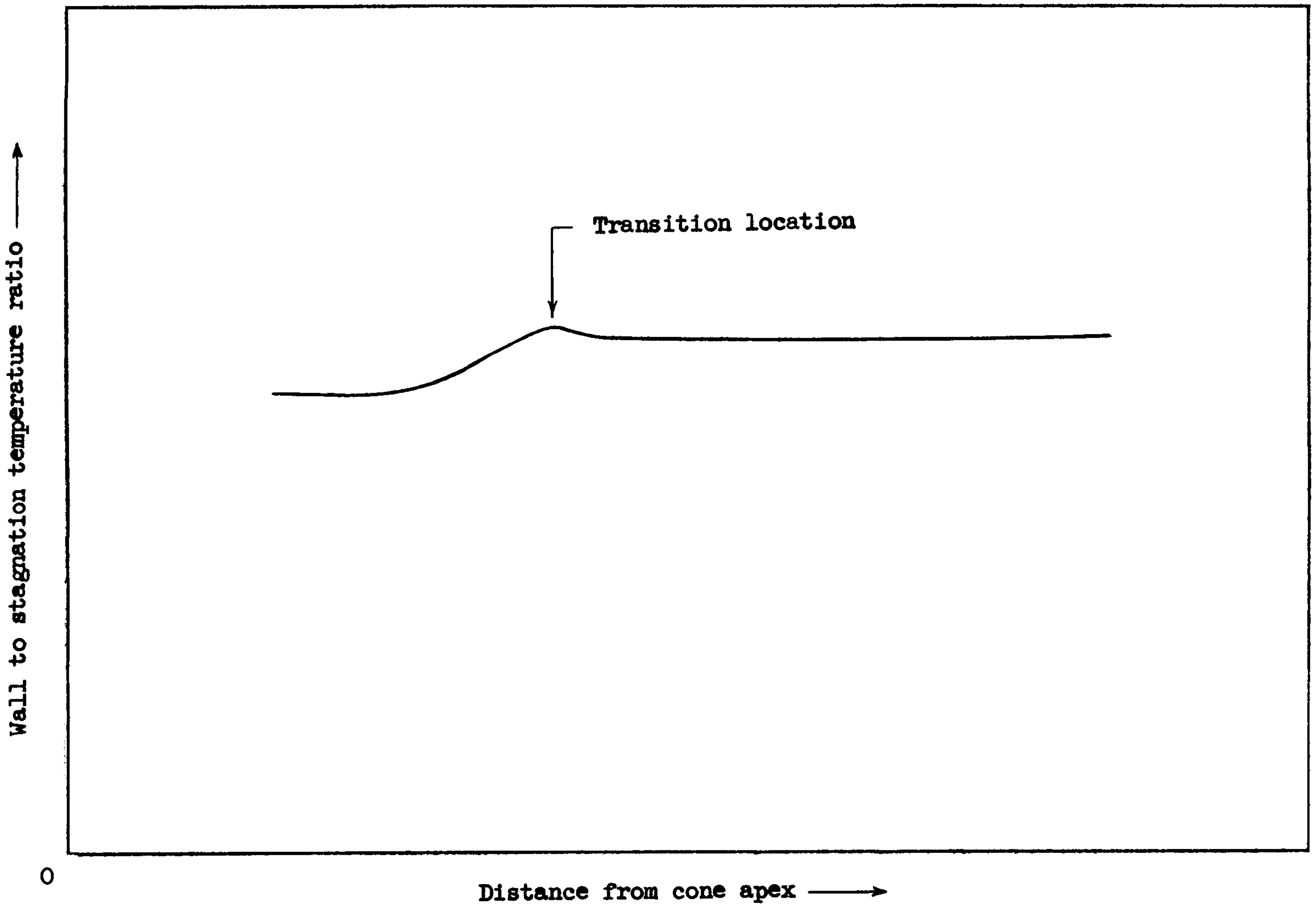

Figure 7.- Sketch of temperature distribution showing method of determining location of transition.

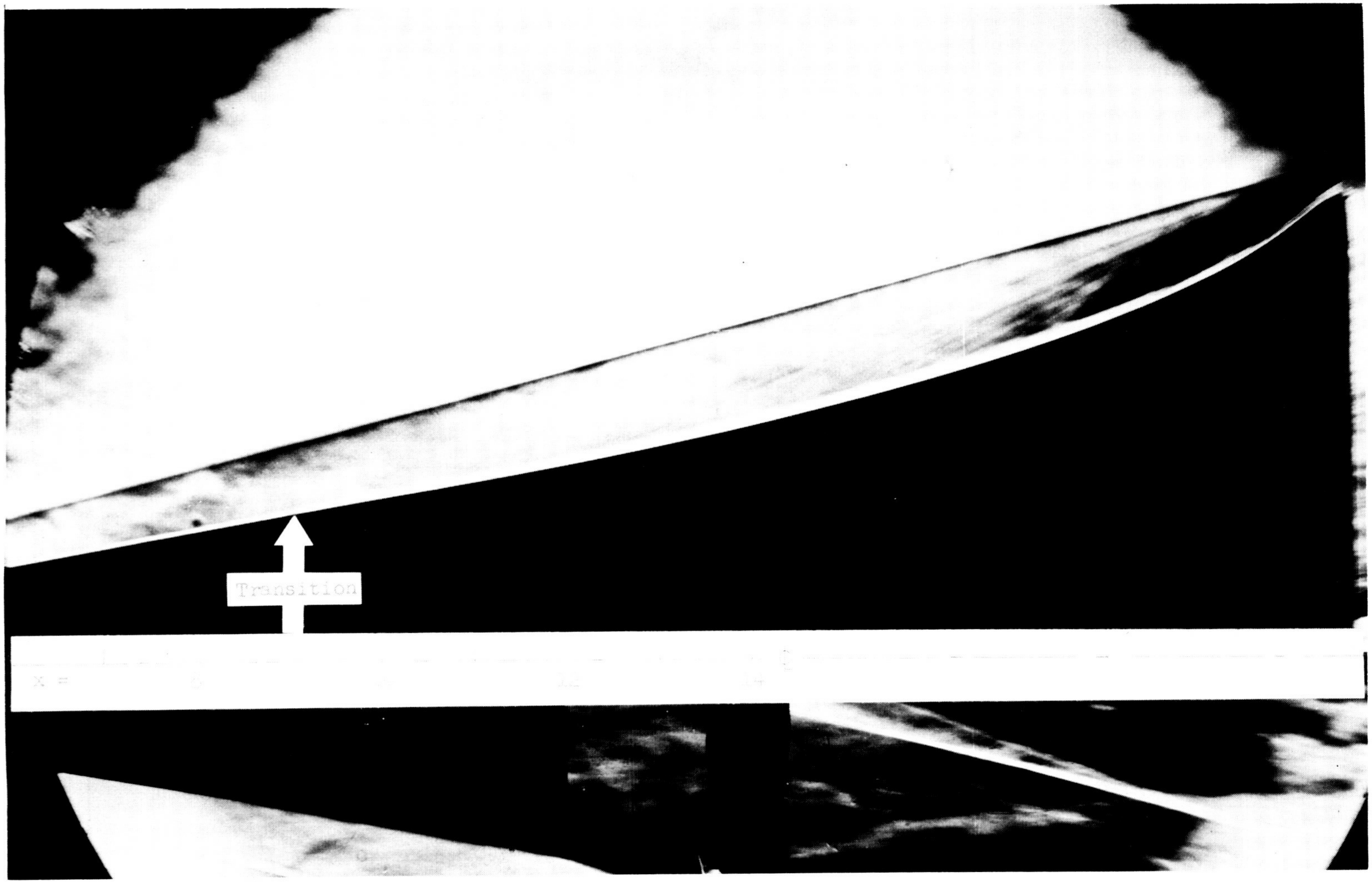

(a) $r_n = 0$; $\sigma = 10^{\circ}$. L-65-73

Figure 8.- Schlieren photographs showing boundary-layer transition (denoted by arrow).

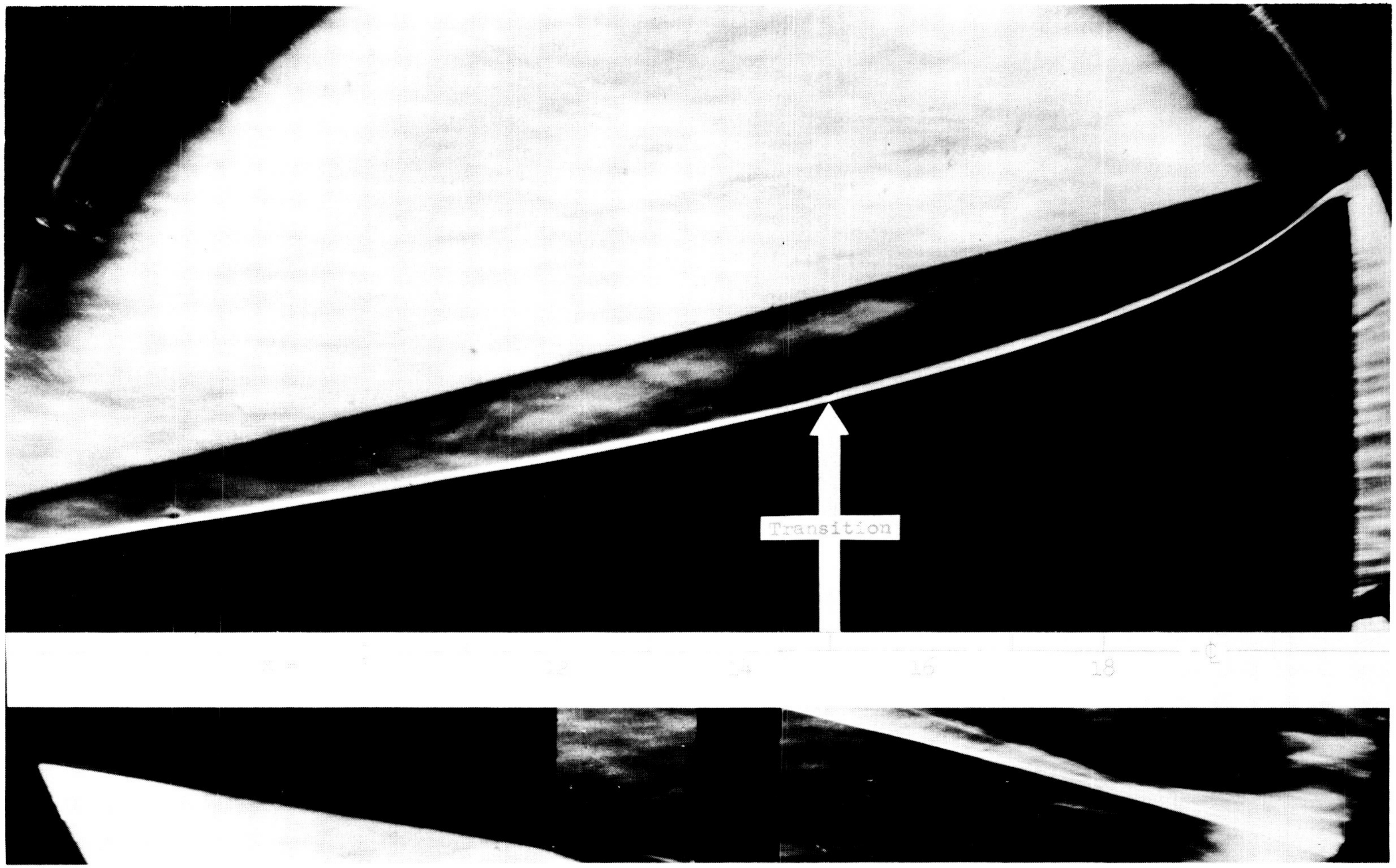

(b) $r_n = 0.14$ in; $\sigma = 10^\circ$. L-65-74

Figure 8.- Continued.

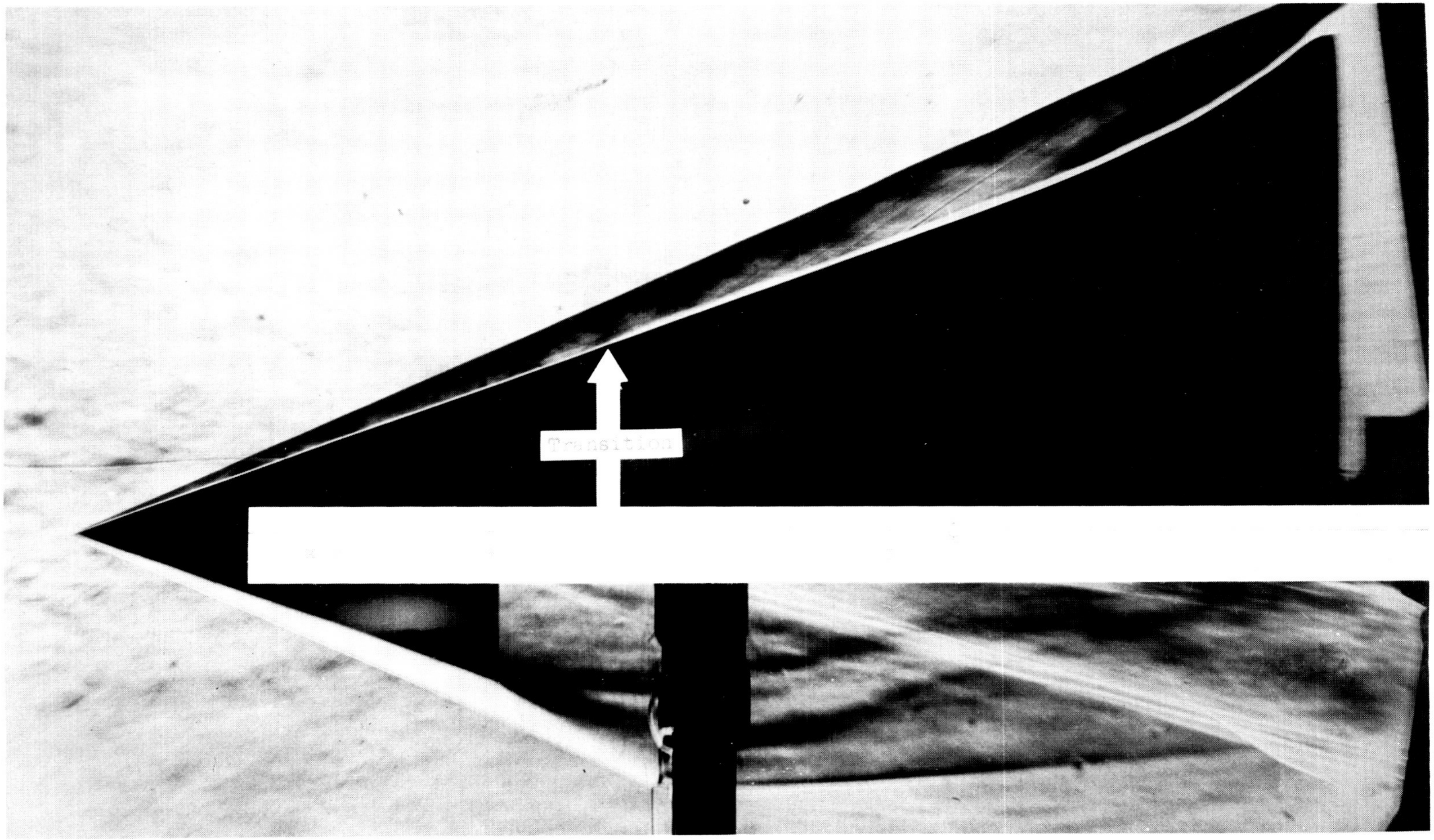

(c) $r_n = 0$; $\sigma = 20^\circ$.

L-65-75

Figure 8.- Concluded.

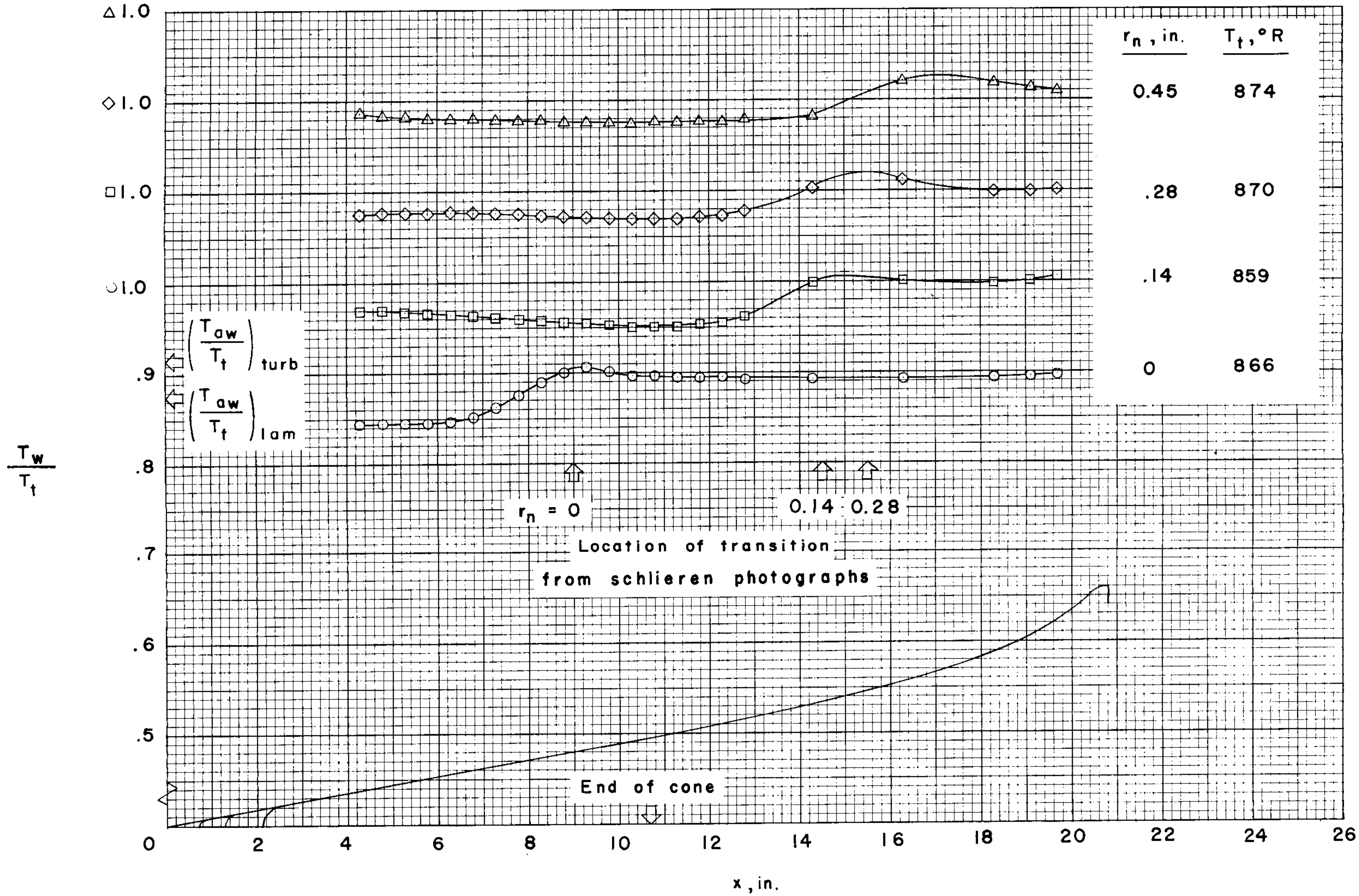

(a) $\sigma = 10^{\circ}$.

Figure 9.- Effect of nose bluntness on model temperature distributions, k = 0.

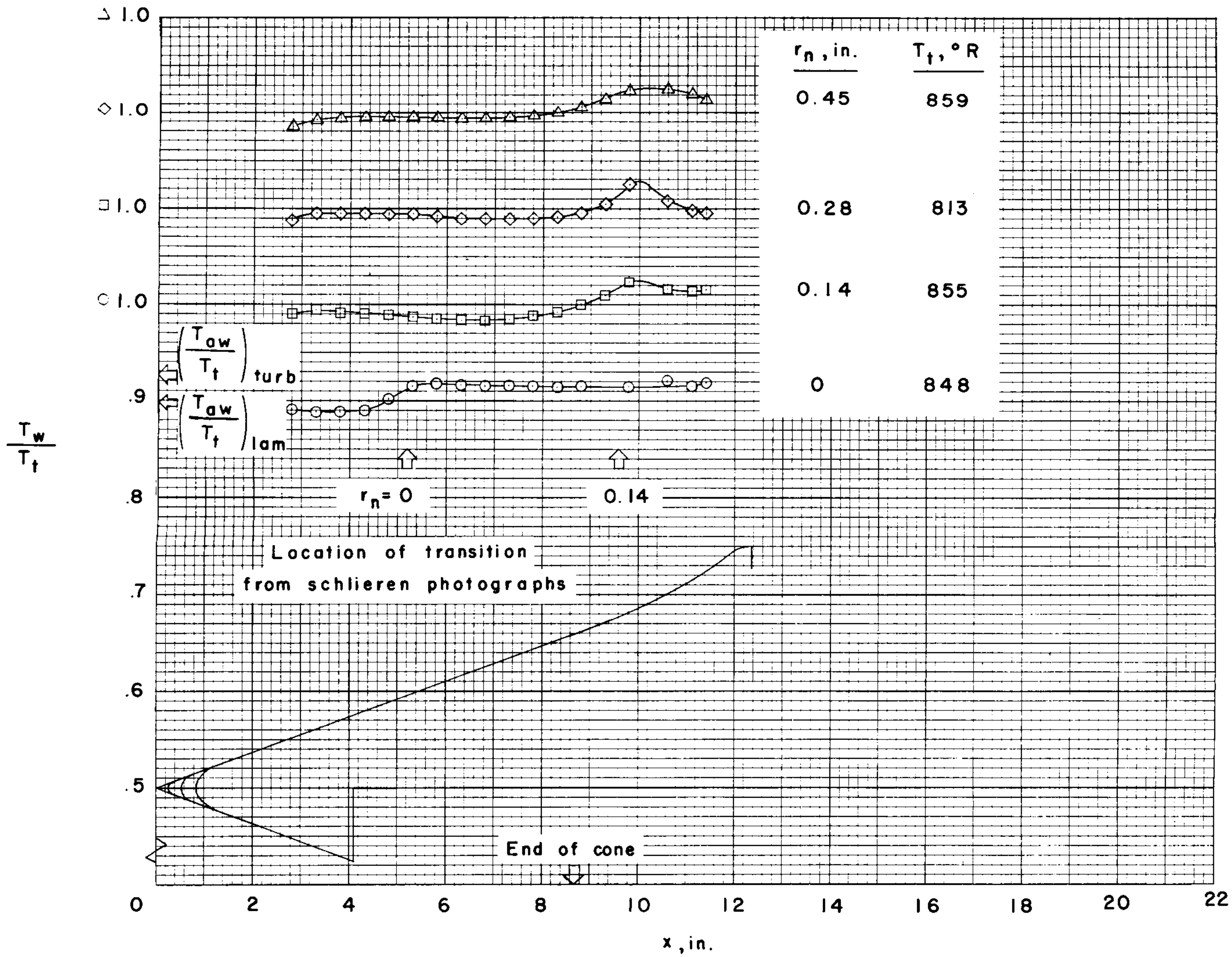

(b) σ = 20°.

Figure 9.- Concluded.

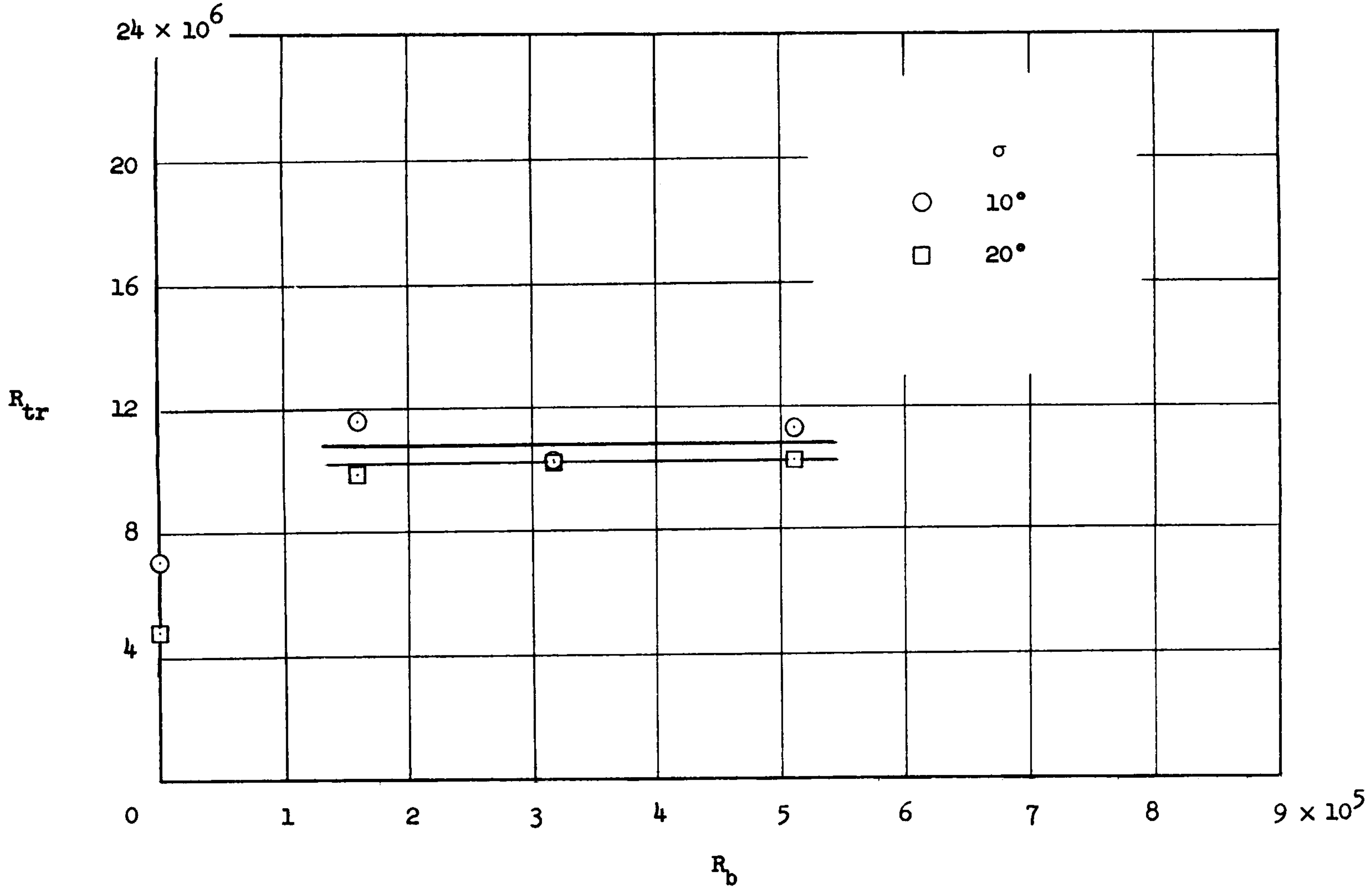

Figure 10.- Transition Reynolds number for configurations investigated.

$r_n = 0$

$r_n = 0.14$ in.

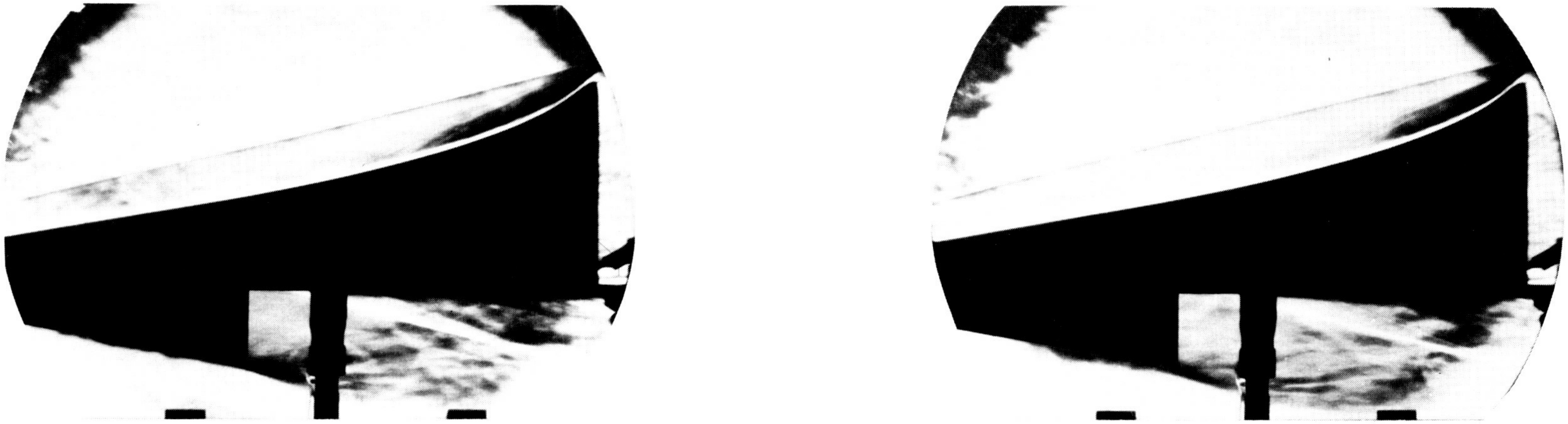

$r_n = 0.28$ in.

$r_n = 0.45$ in.

(a) $\sigma = 10^{\circ}$.

L-65-76

Figure 11.- Schlieren photographs of model; k = 0.

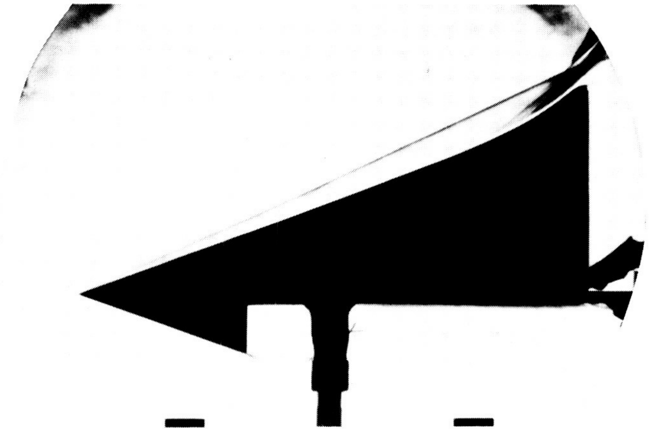

$r_n = 0$

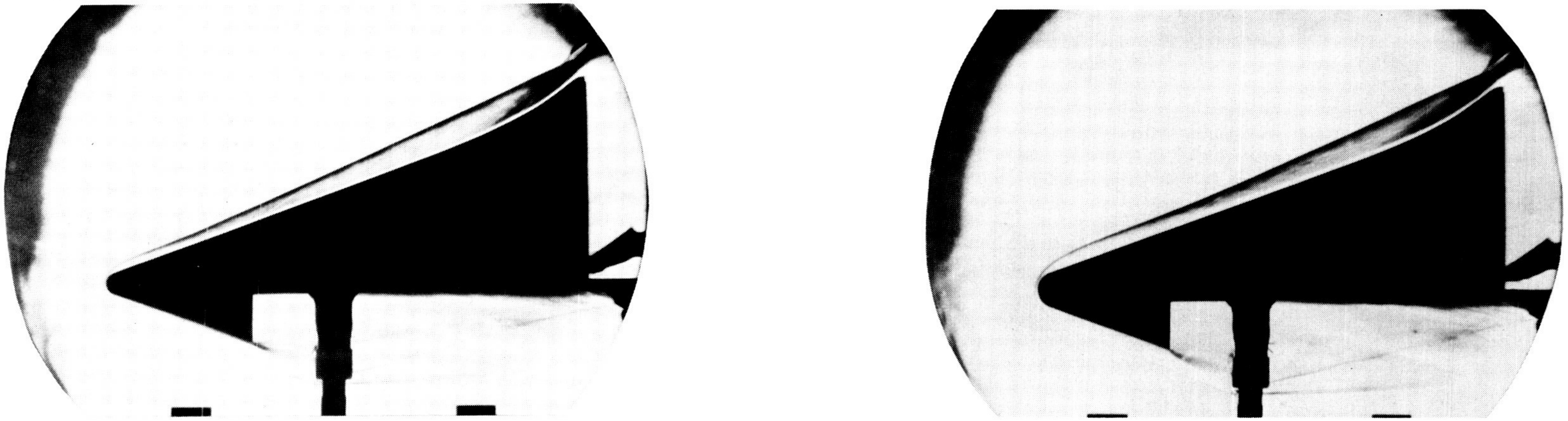

$r_n = 0.28$ in.

$r_n = 0.45$ in.

(b) $\sigma = 20^{\circ}$.

L-65-77

Figure 11.- Concluded.

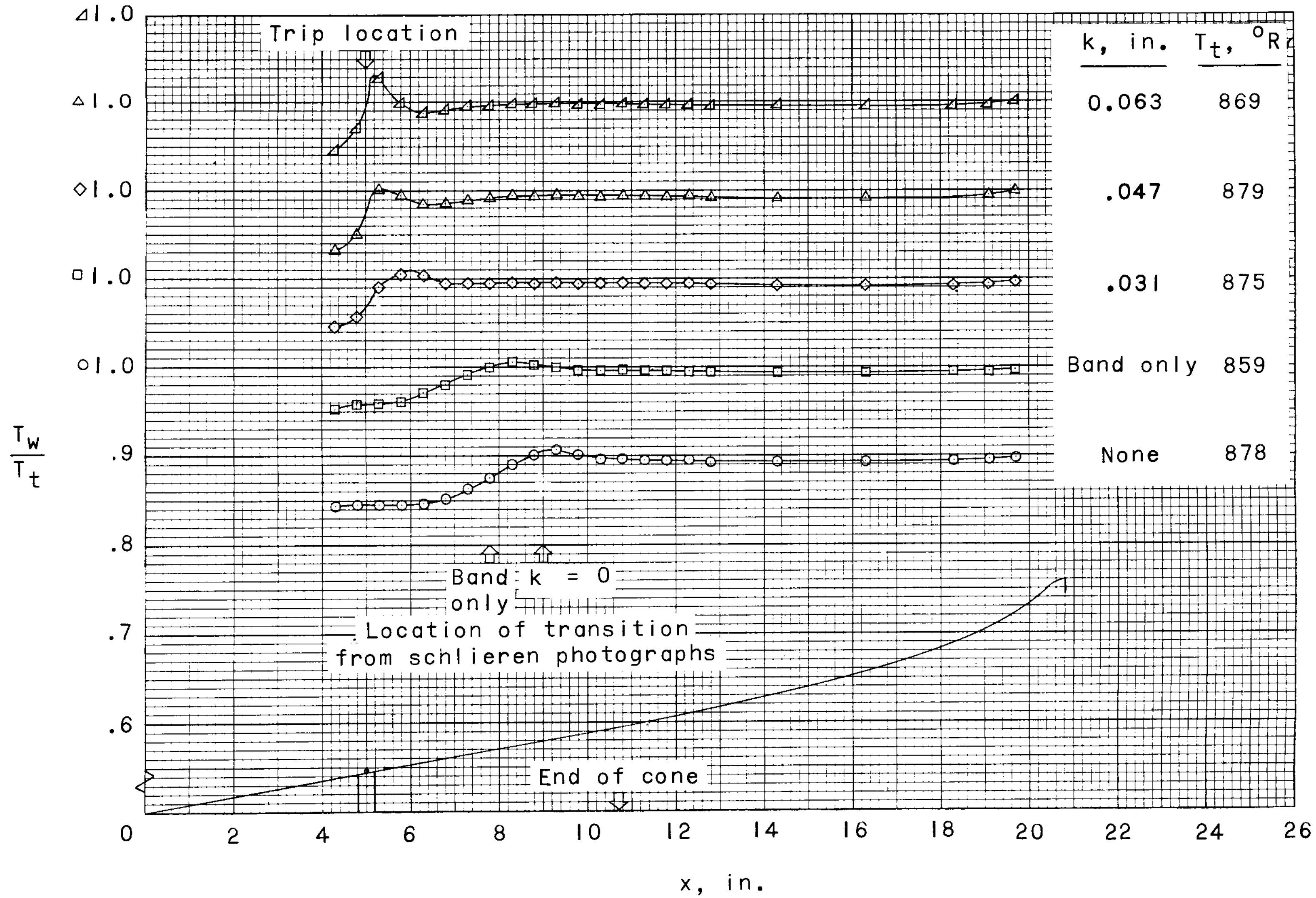

(a) $r_n = 0$.

Figure 12.- Effect of boundary-layer roughness size on model temperature distributions; $\sigma = 10^\circ$.

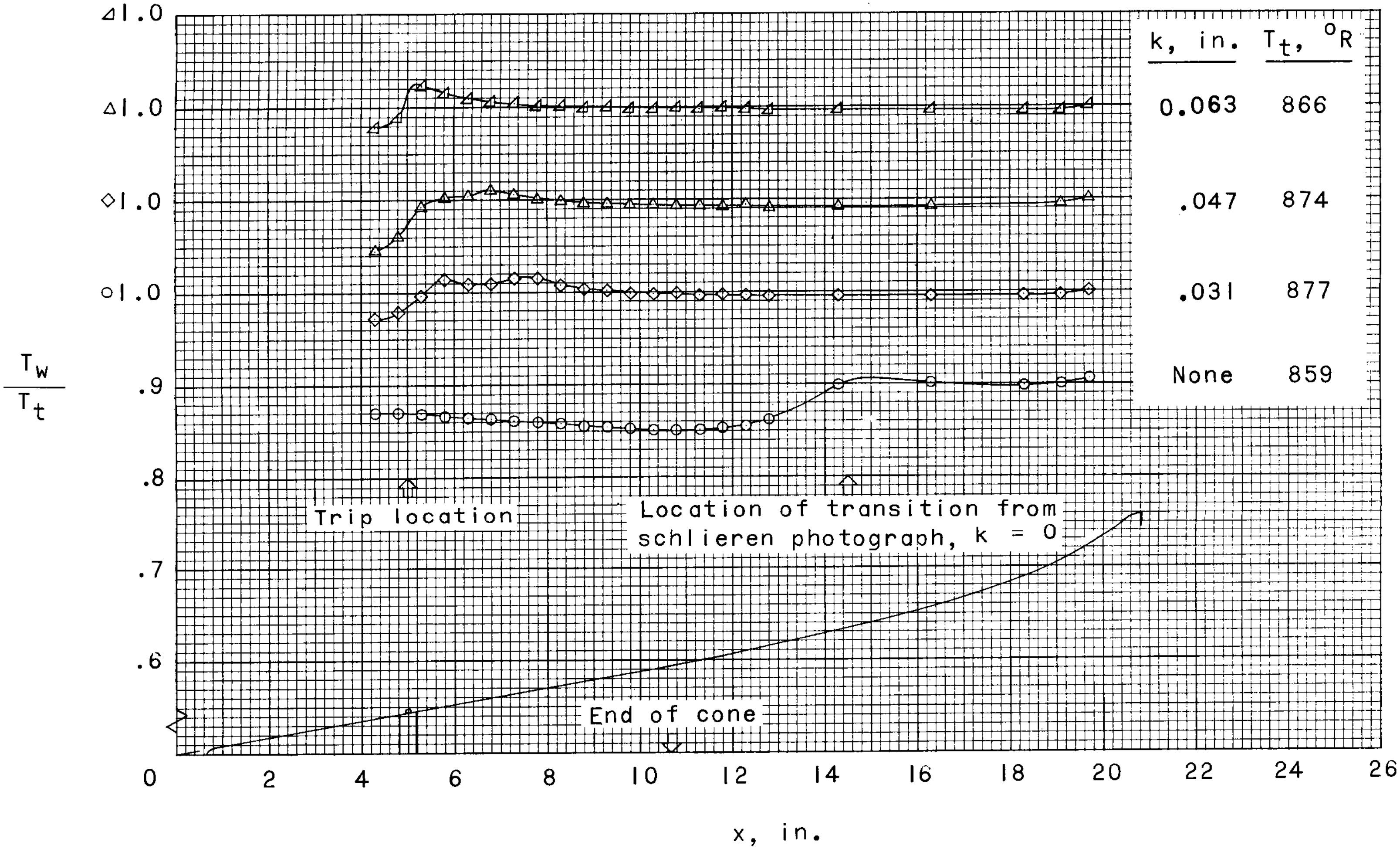

(b) $r_n = 0.14$ in.

Figure 12.- Continued.

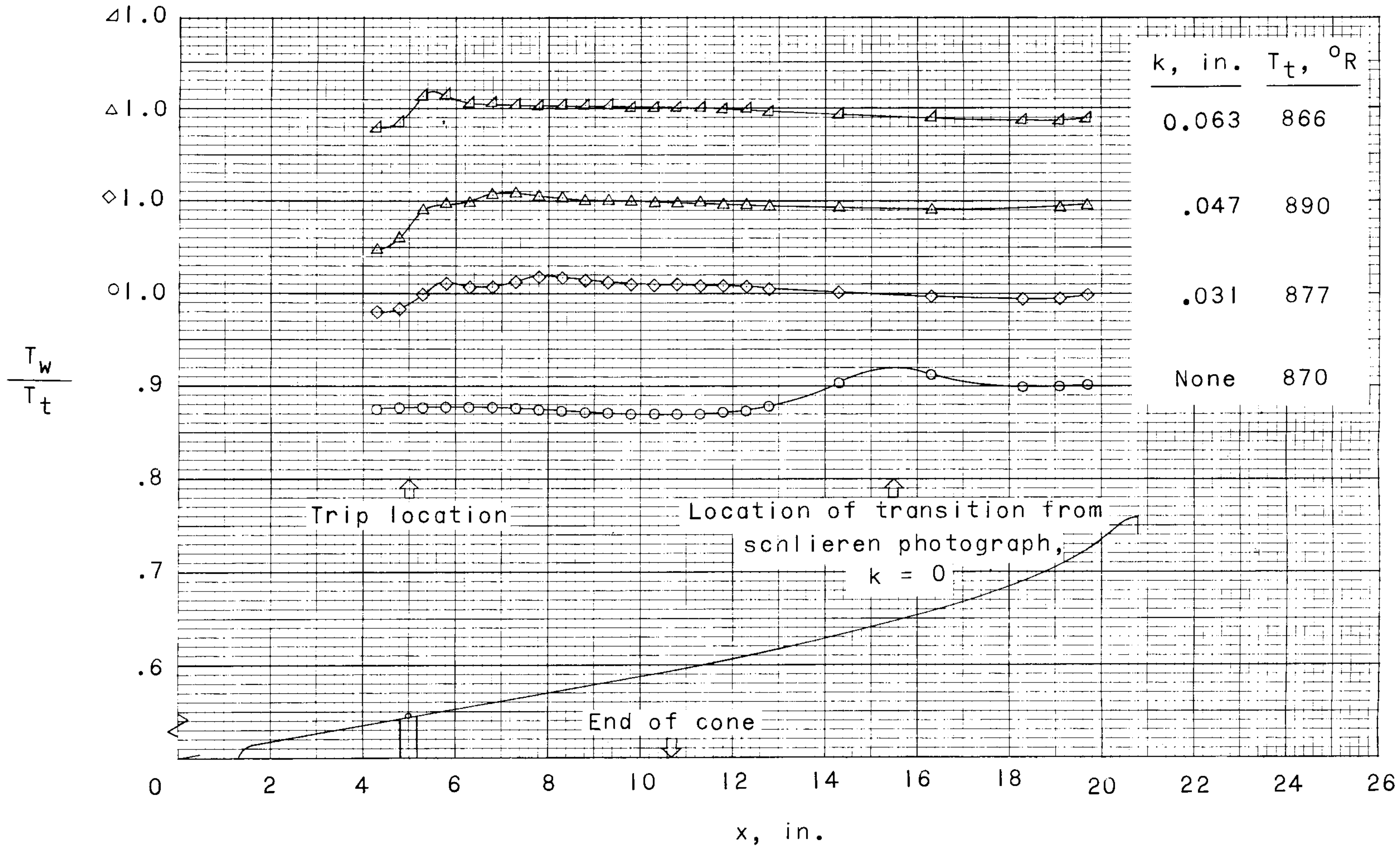

(c) $r_n = 0.28$ in.

Figure 12.- Continued.

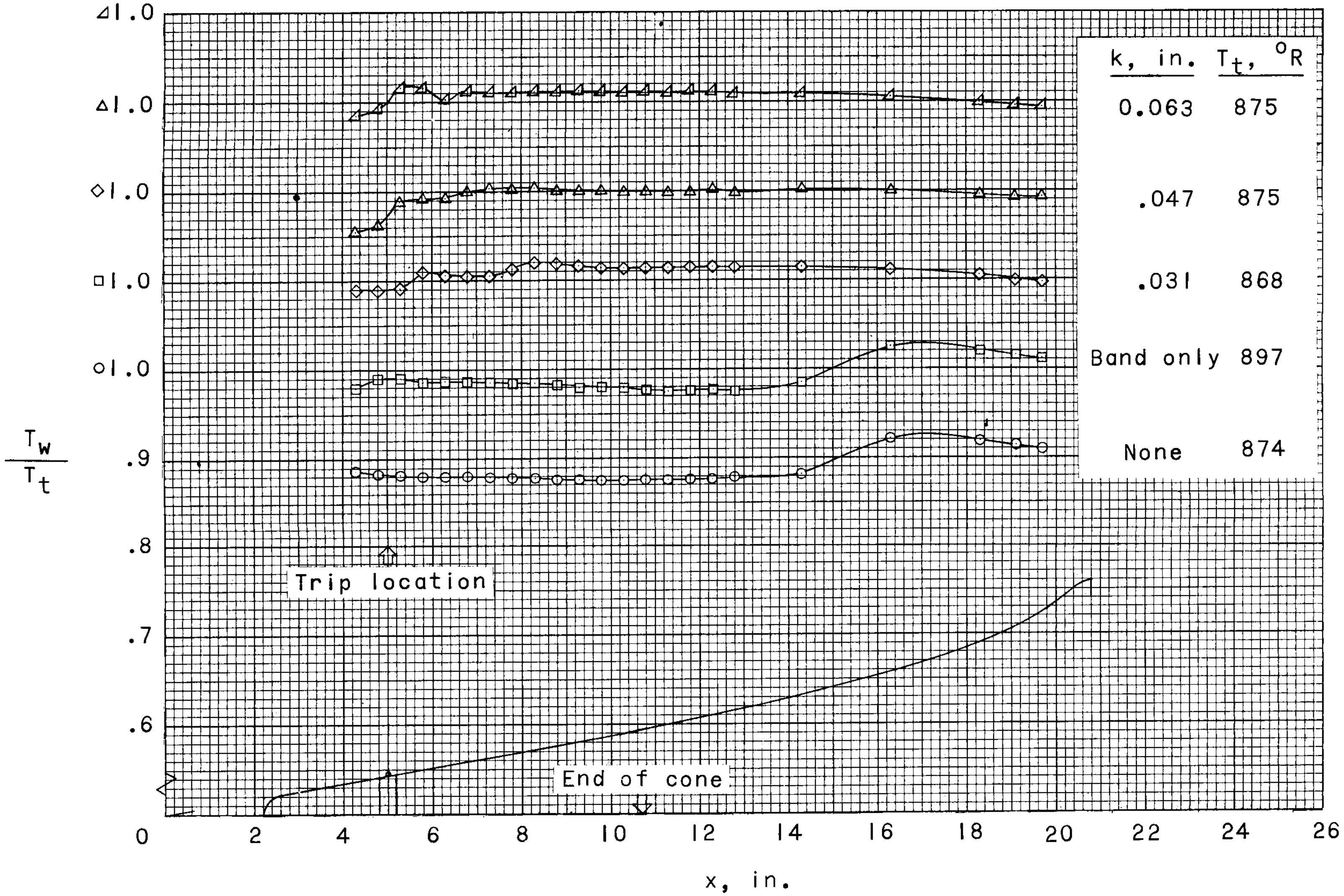

(d) $r_n = 0.45$ in.

Figure 12.- Concluded.

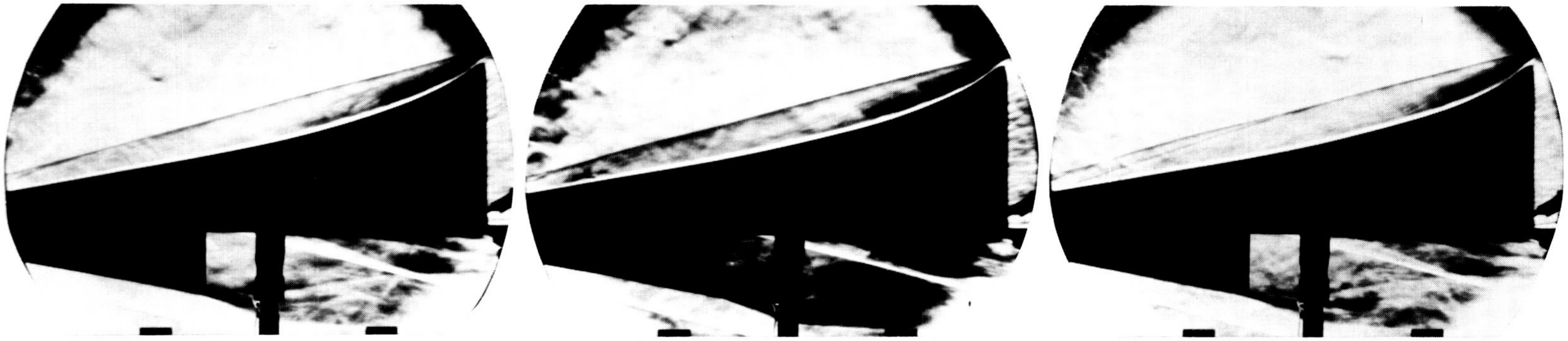

k = 0.031 in.

k = 0.047 in.

k = 0.063 in.

(a) $r_n = 0$.

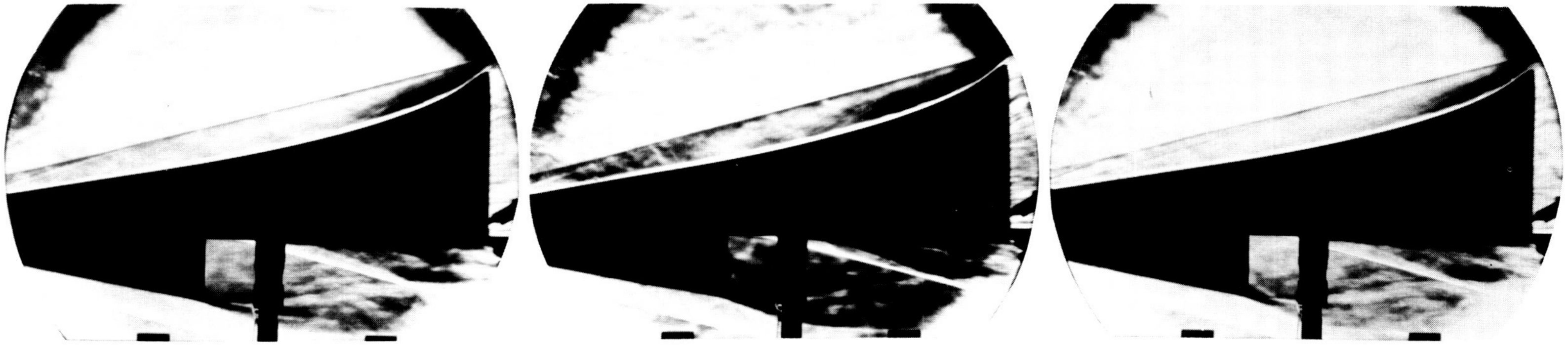

k = 0.031 in.

k = 0.047 in.

k = 0.063 in.

(b) $r_n = 0.14$ in.

L-65-78

Figure 13.- Schlieren photographs of model with boundary layer trip, $\sigma = 10^\circ$.

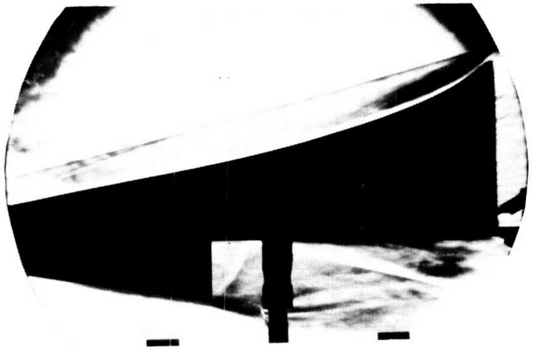

k = 0.031 in.

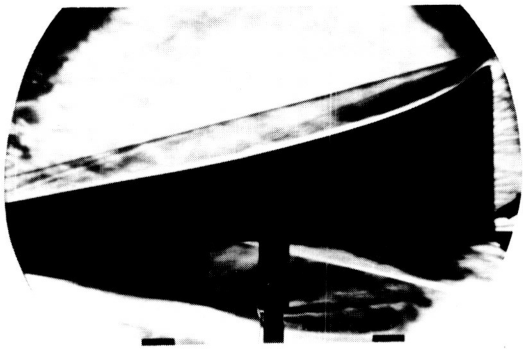

k = 0.047 in.

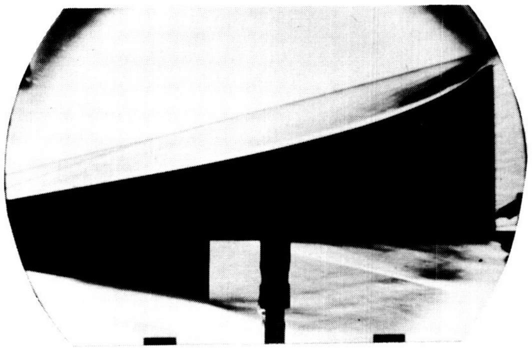

k = 0.063 in.

(c) r_n = 0.28 in.

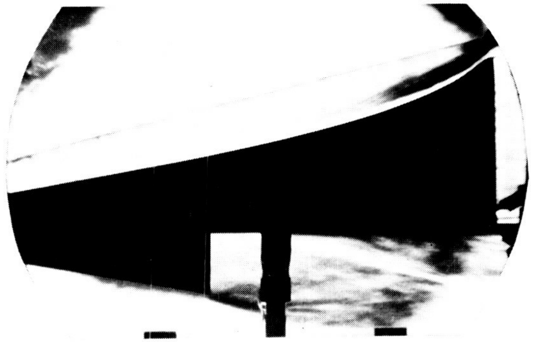

k = 0.031 in.

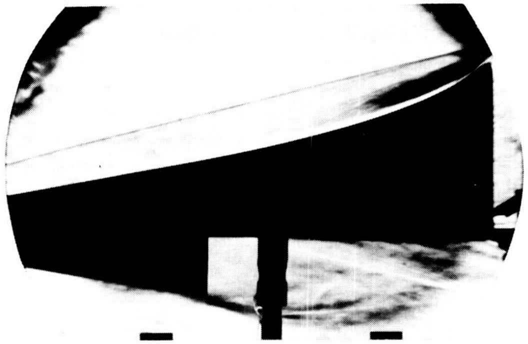

k = 0.047 in.

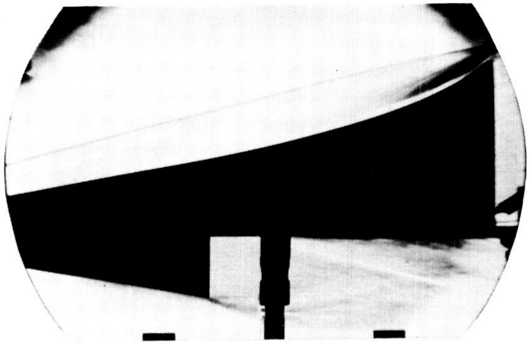

k = 0.063 in.

(d) r_n = 0.45 in.

L-65-79

Figure 13.- Concluded.

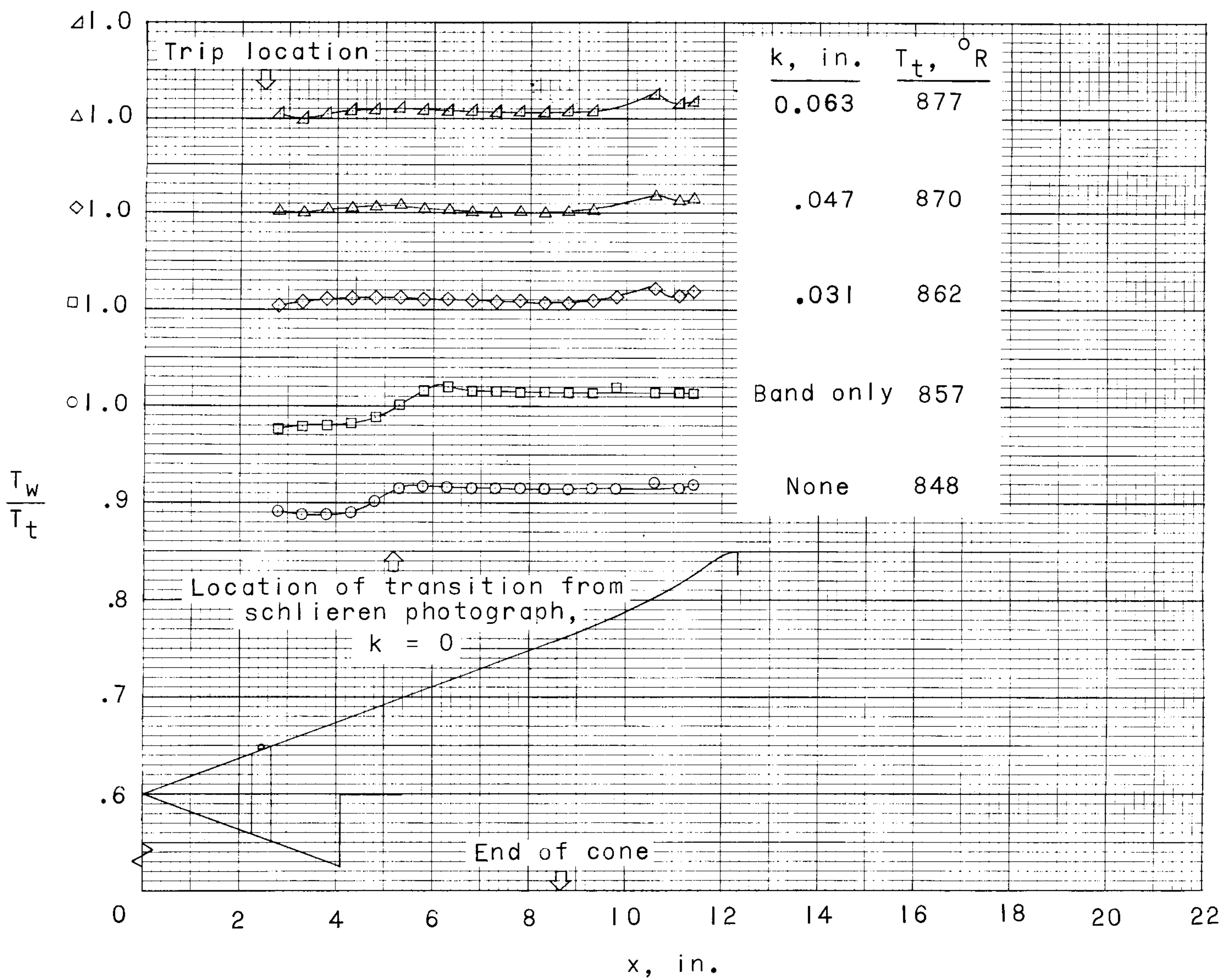

(a) $r_n = 0$.

Figure 14.- Effect of boundary-layer roughness size on model temperature distributions; $\sigma = 20^{\circ}$.

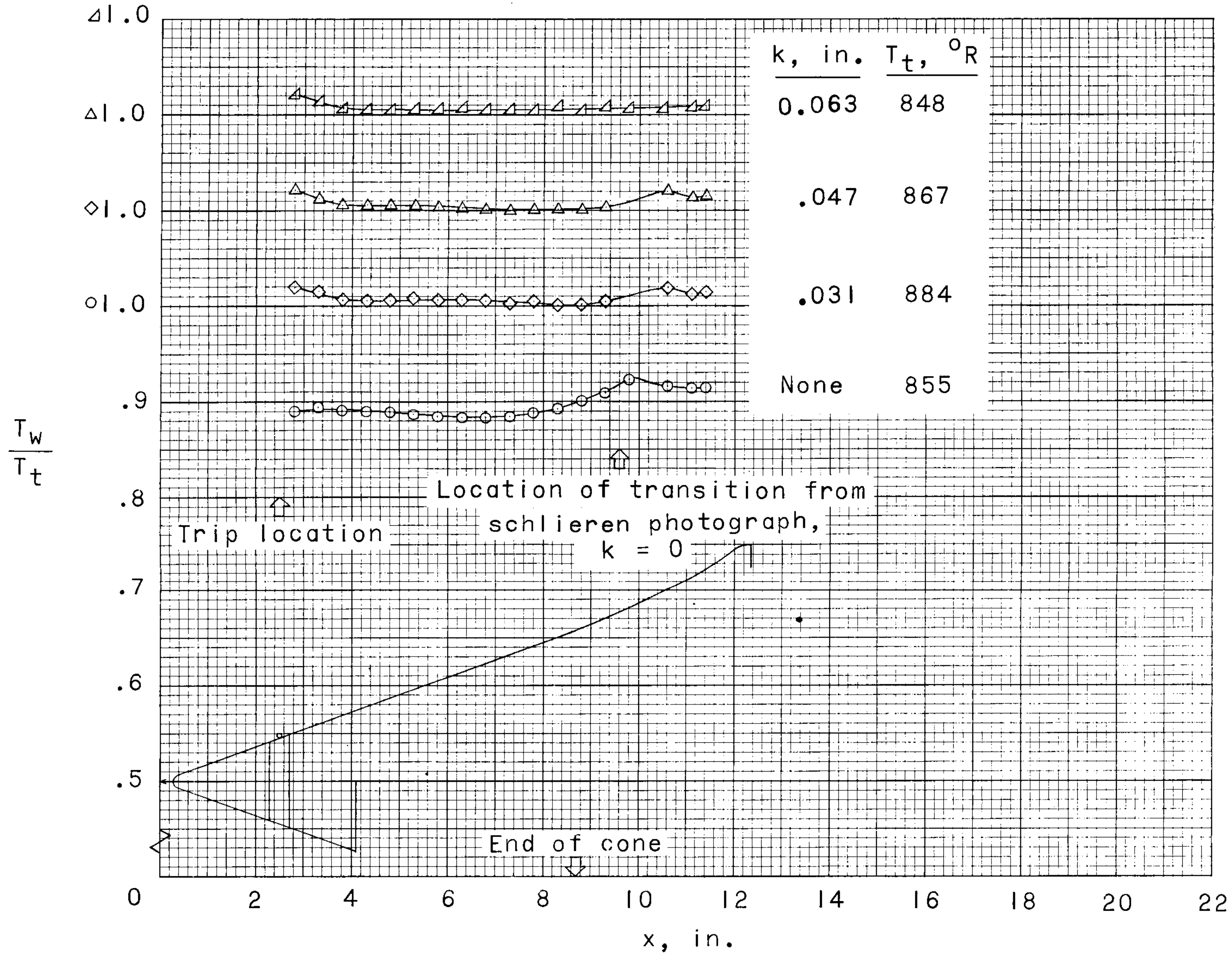

(b) $r_n = 0.14$ in.

Figure 14.- Continued.

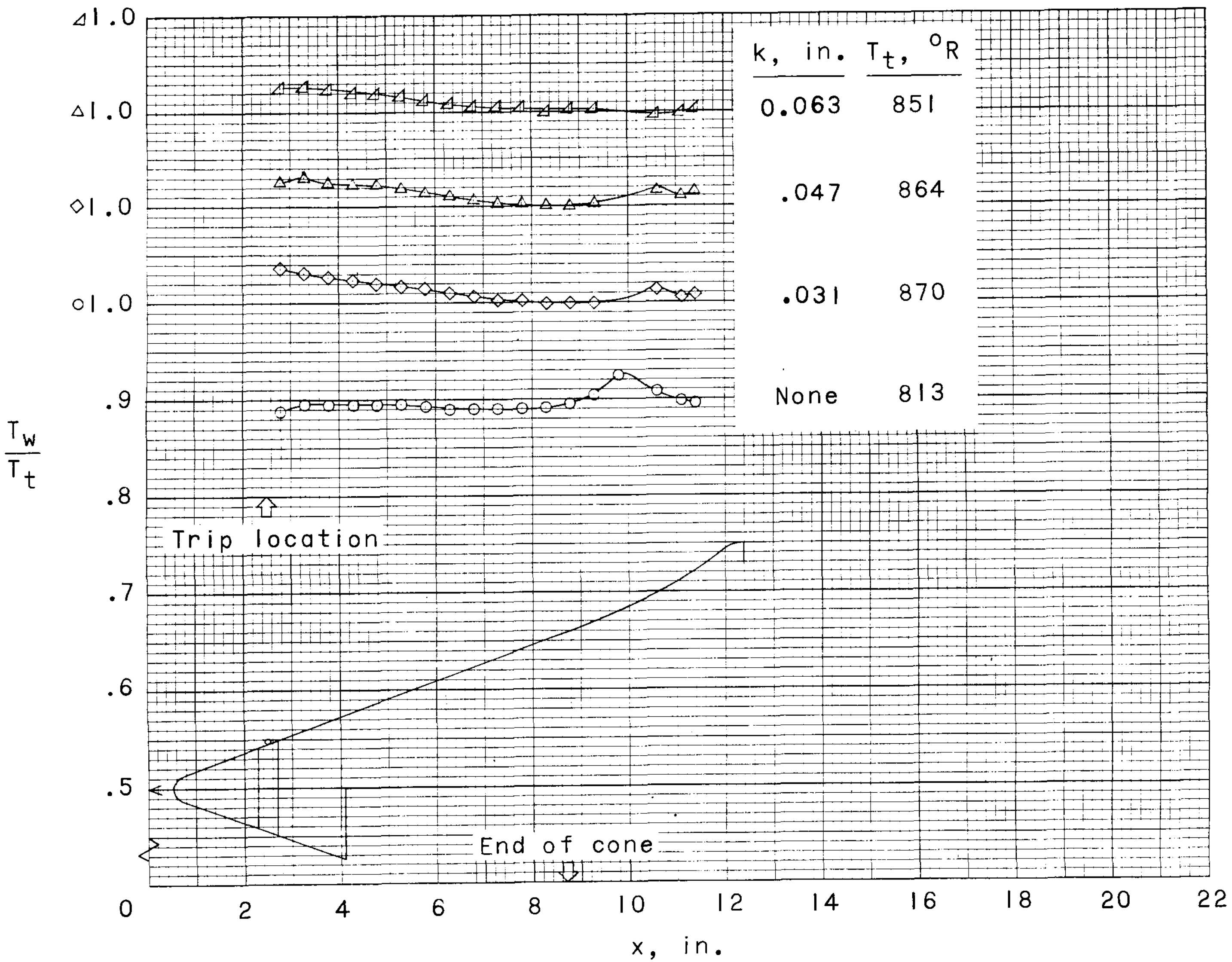

(c) r_n = 0.28 in.

Figure 14.- Continued.

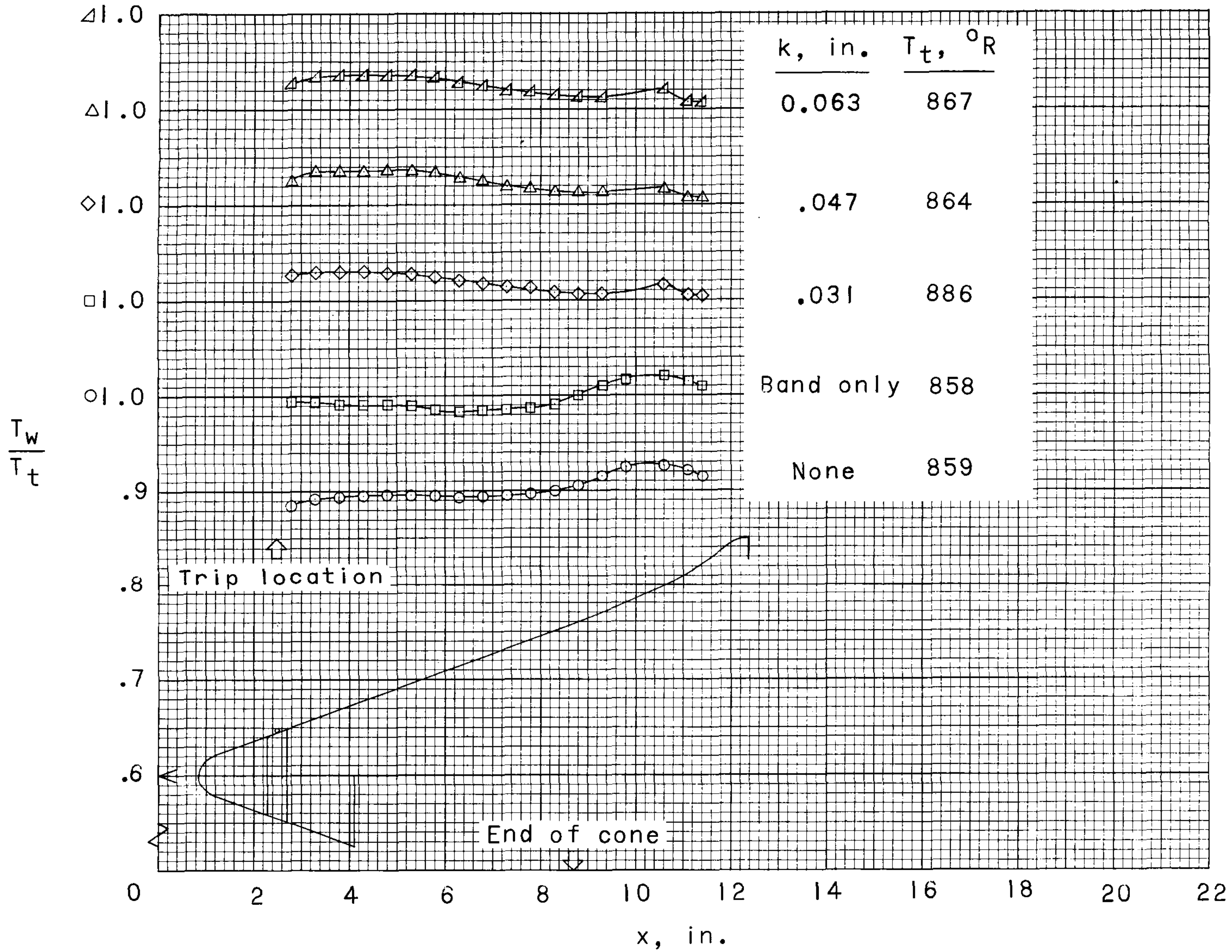

(d) $r_n = 0.45$ in.

Figure 14.- Concluded.

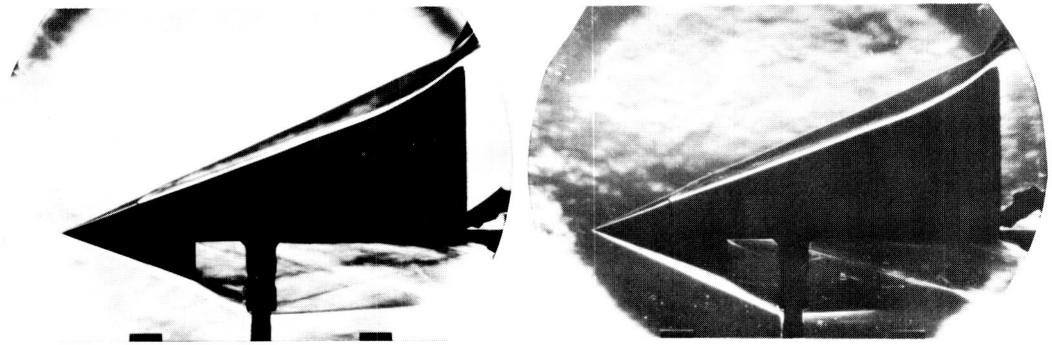

k = 0.047 in.

k = 0.063 in.

(a) $r_n = 0$.

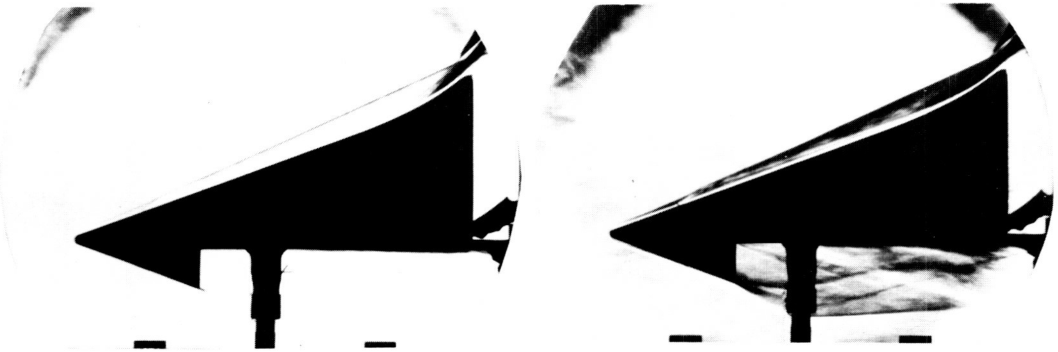

k = 0.031 in.

k = 0.047 in.

(b) $r_n = 0.14$ in.

L-65-80

Figure 15.- Schlieren photographs of model with boundary layer trip; $\sigma = 20^\circ$.

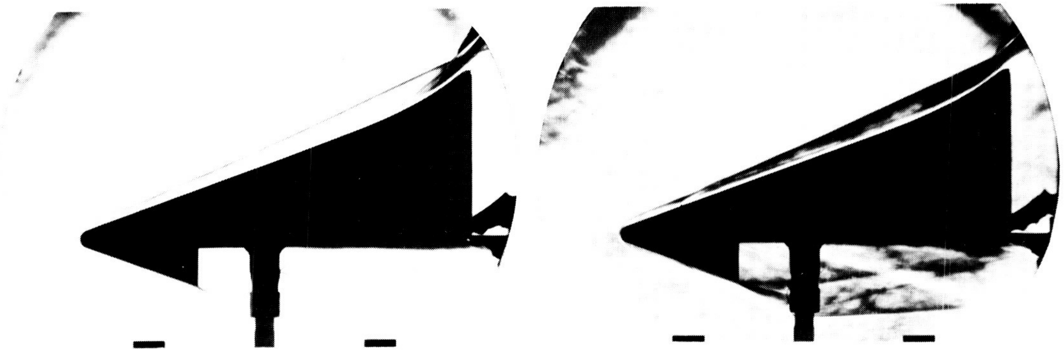

k = 0.031 in.

k = 0.047 in.

(c) $r_n = 0.28$ in.

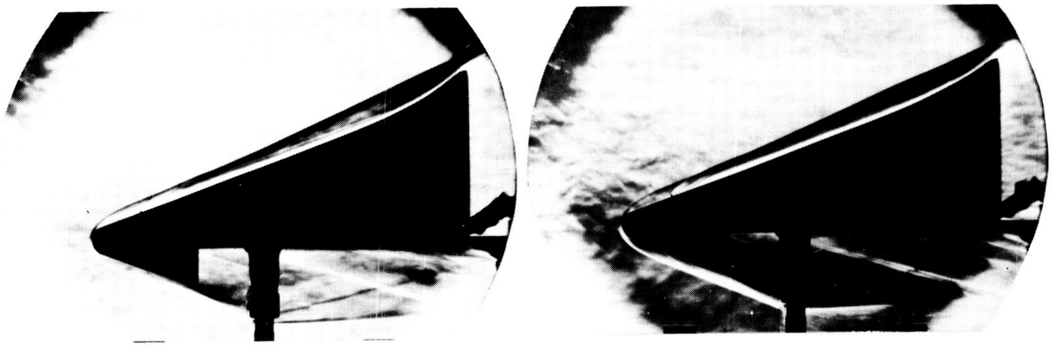

k = 0.047 in.

k = 0.063 in.

(d) $r_n = 0.45$ in.

L-65-81

Figure 15.- Concluded.

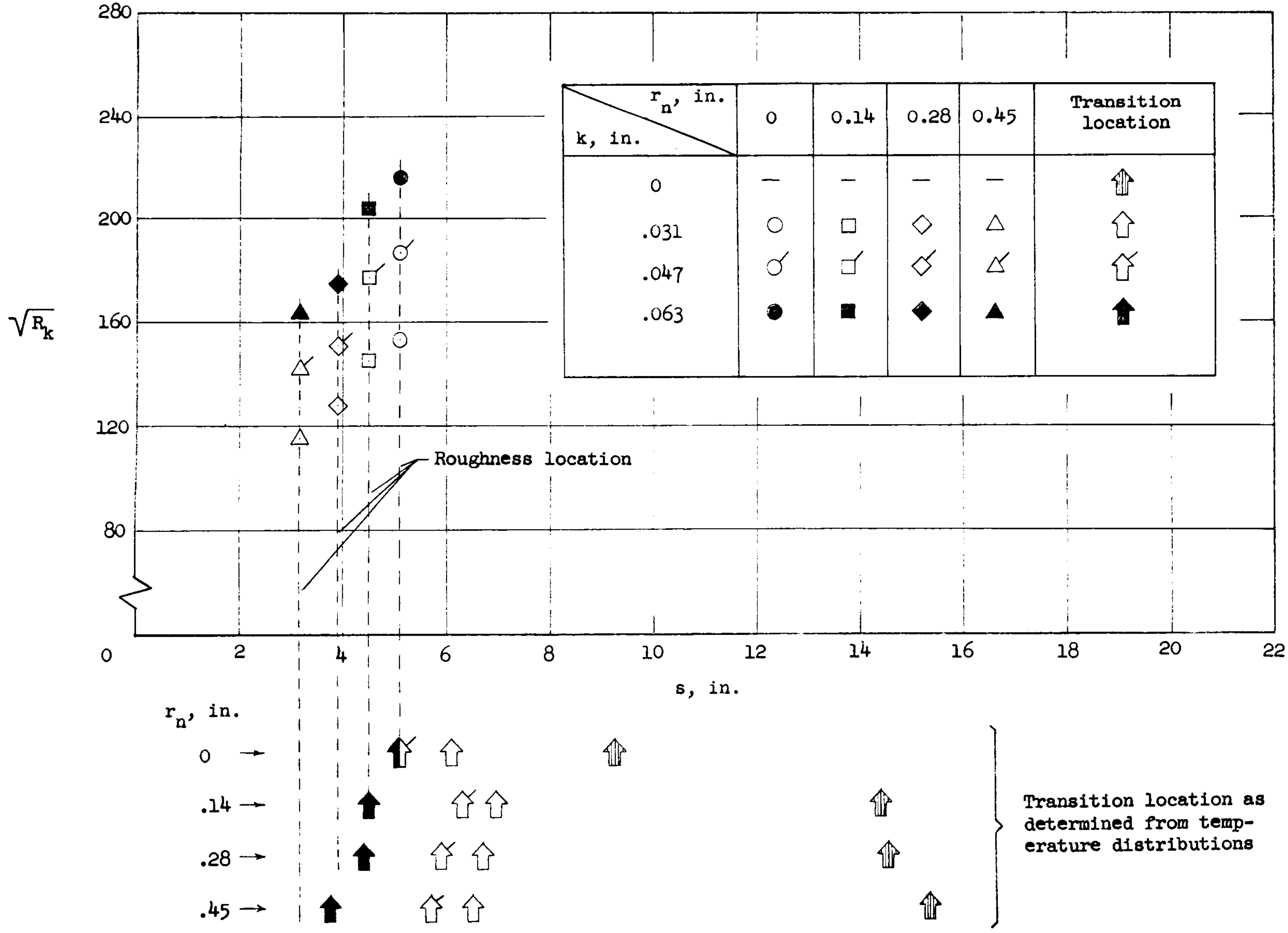

Figure 16.- Summary of roughness Reynolds number and transition locations for configurations with roughness; $\sigma = 10^{\circ}$.

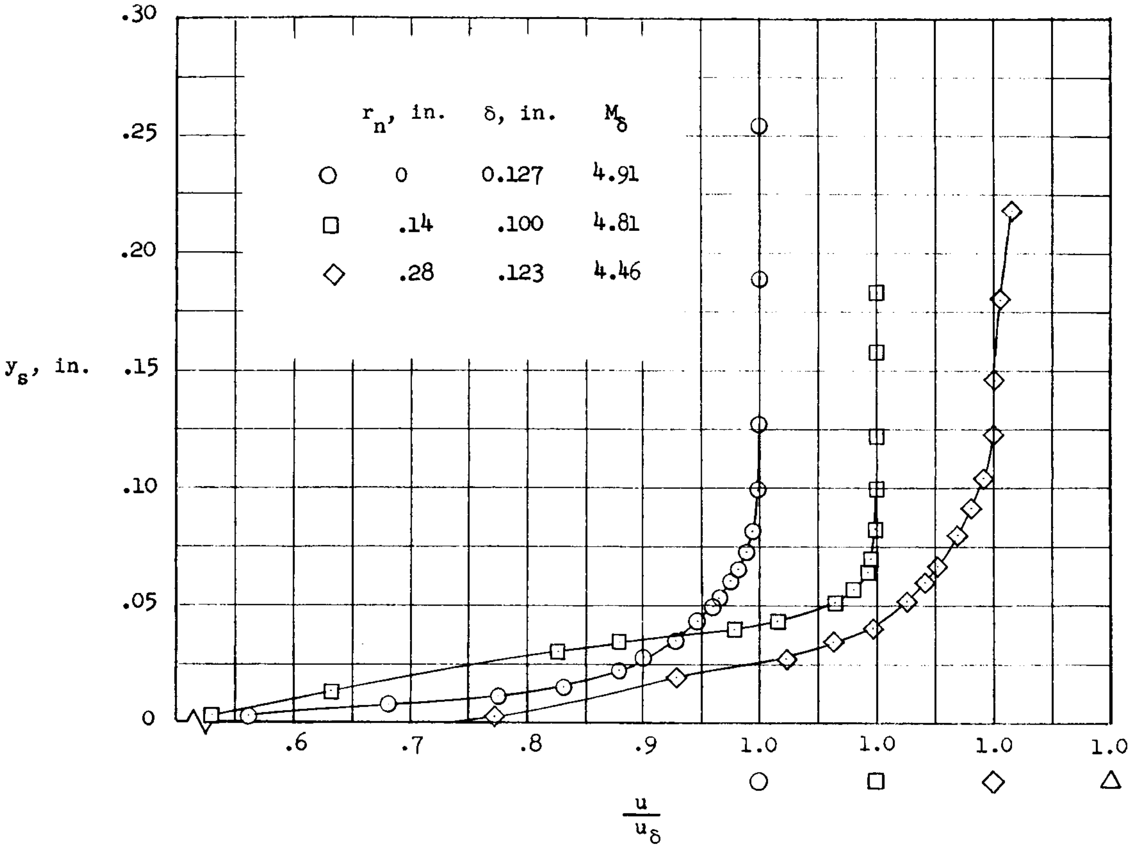

(a) Forward survey station 1, x = 10.55 in.

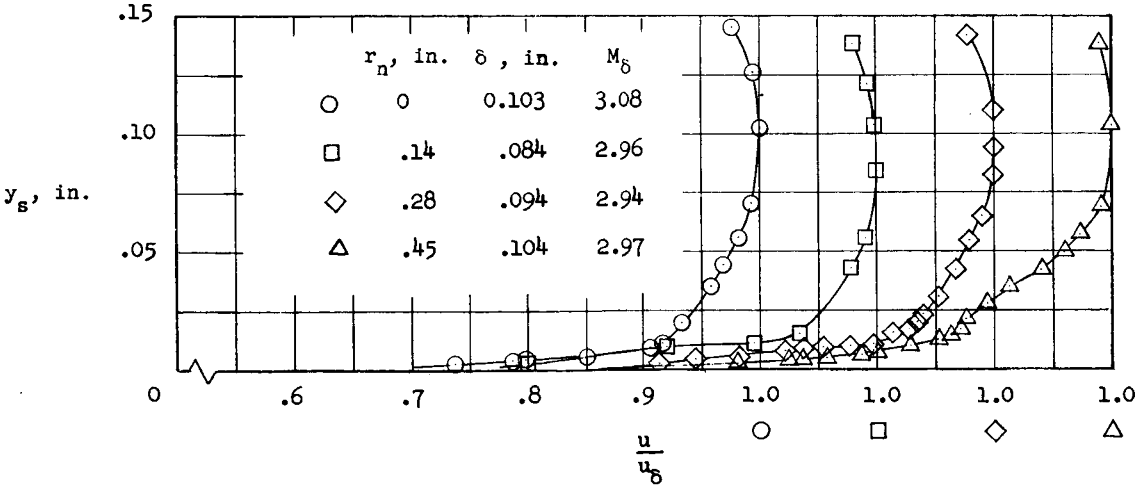

(b) Rearward survey station 2, x = 19.87 in.

Figure 17.- Boundary-layer velocity profiles; $\sigma = 10^{\circ}$; k = 0.

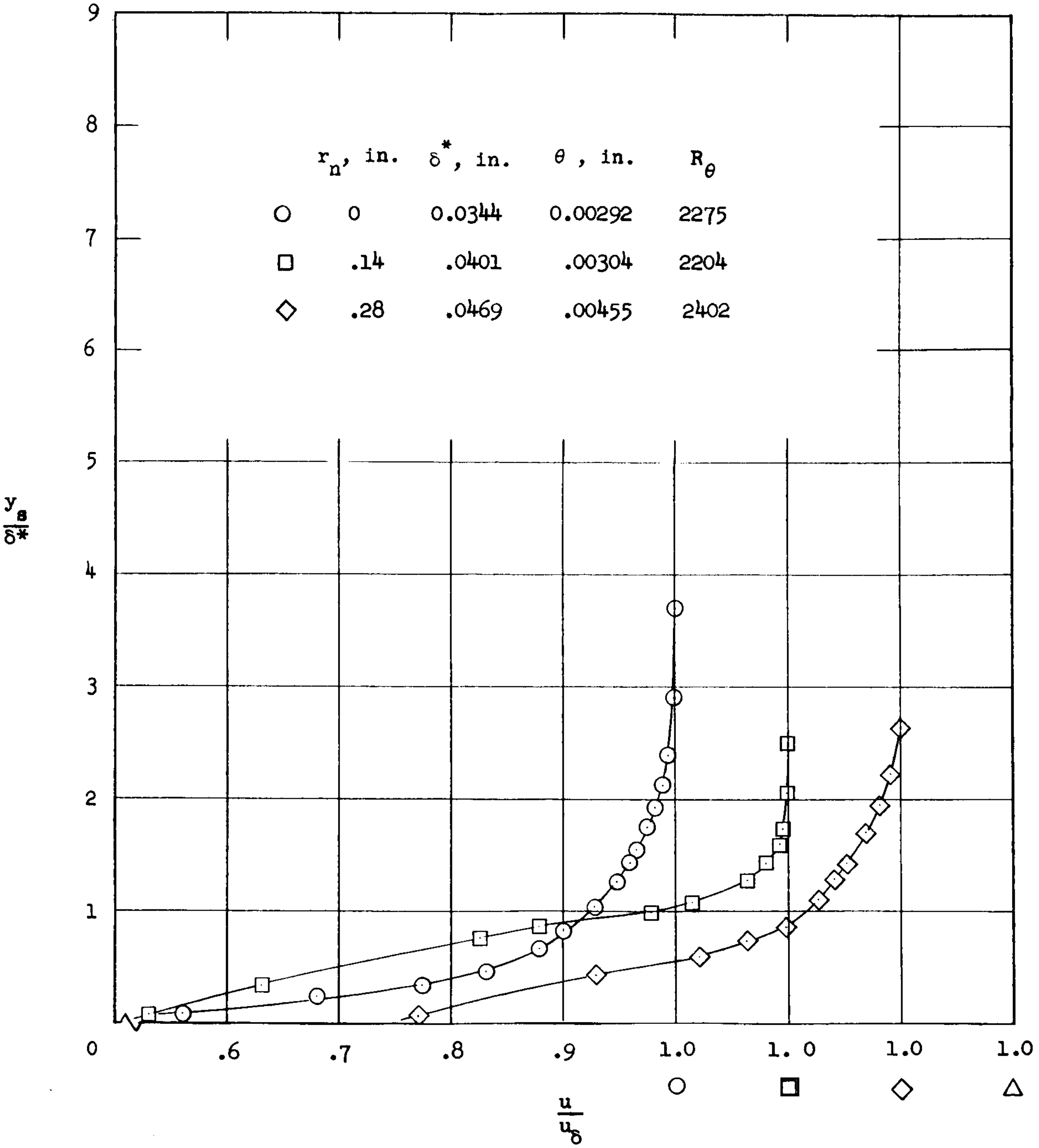

(a) Forward survey station, $x = 10.55$ in.

Figure 18.- Nondimensional velocity profiles, $\sigma = 10^\circ$, $k = 0$.

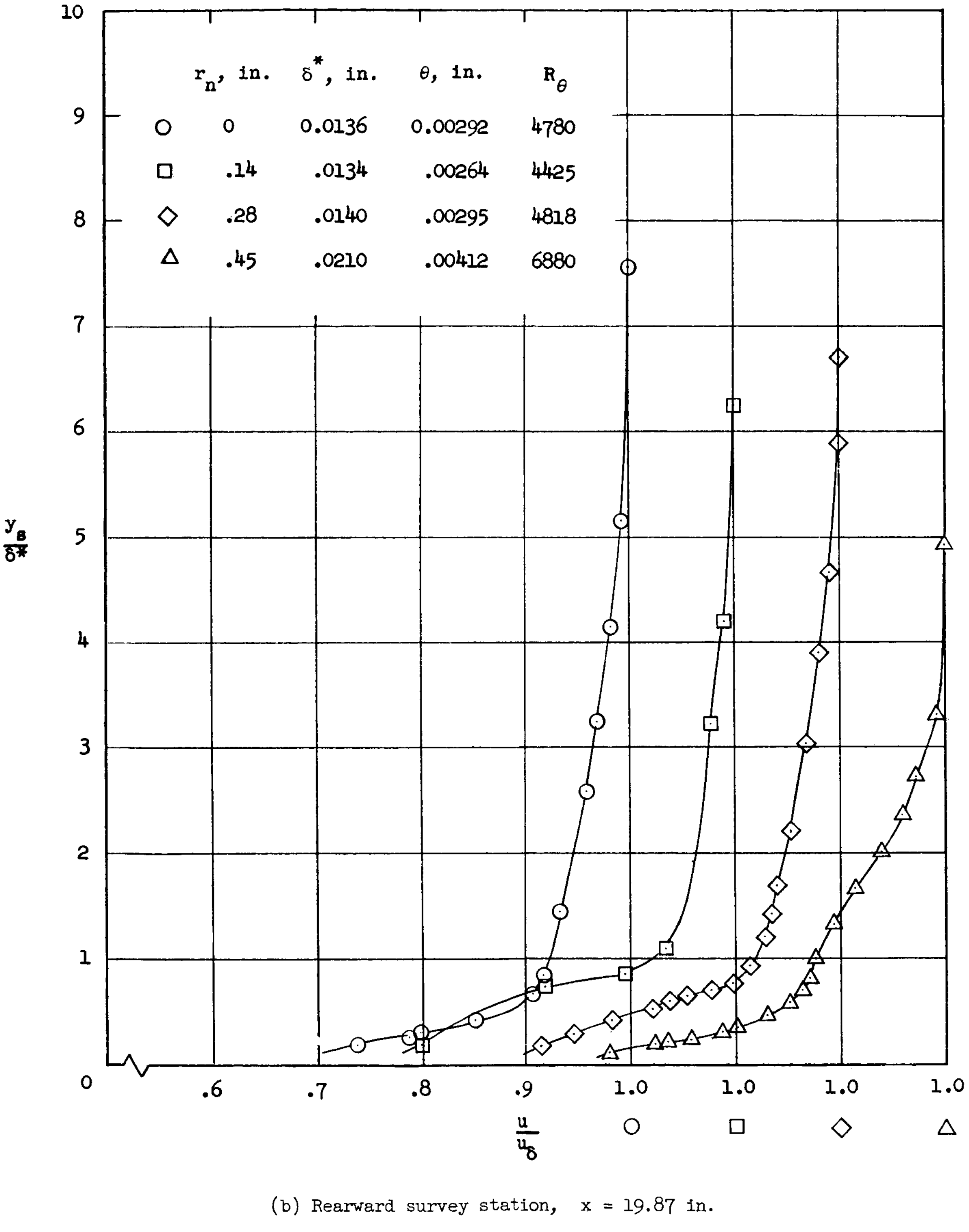

(b) Rearward survey station, x = 19.87 in.

Figure 18.- Concluded.

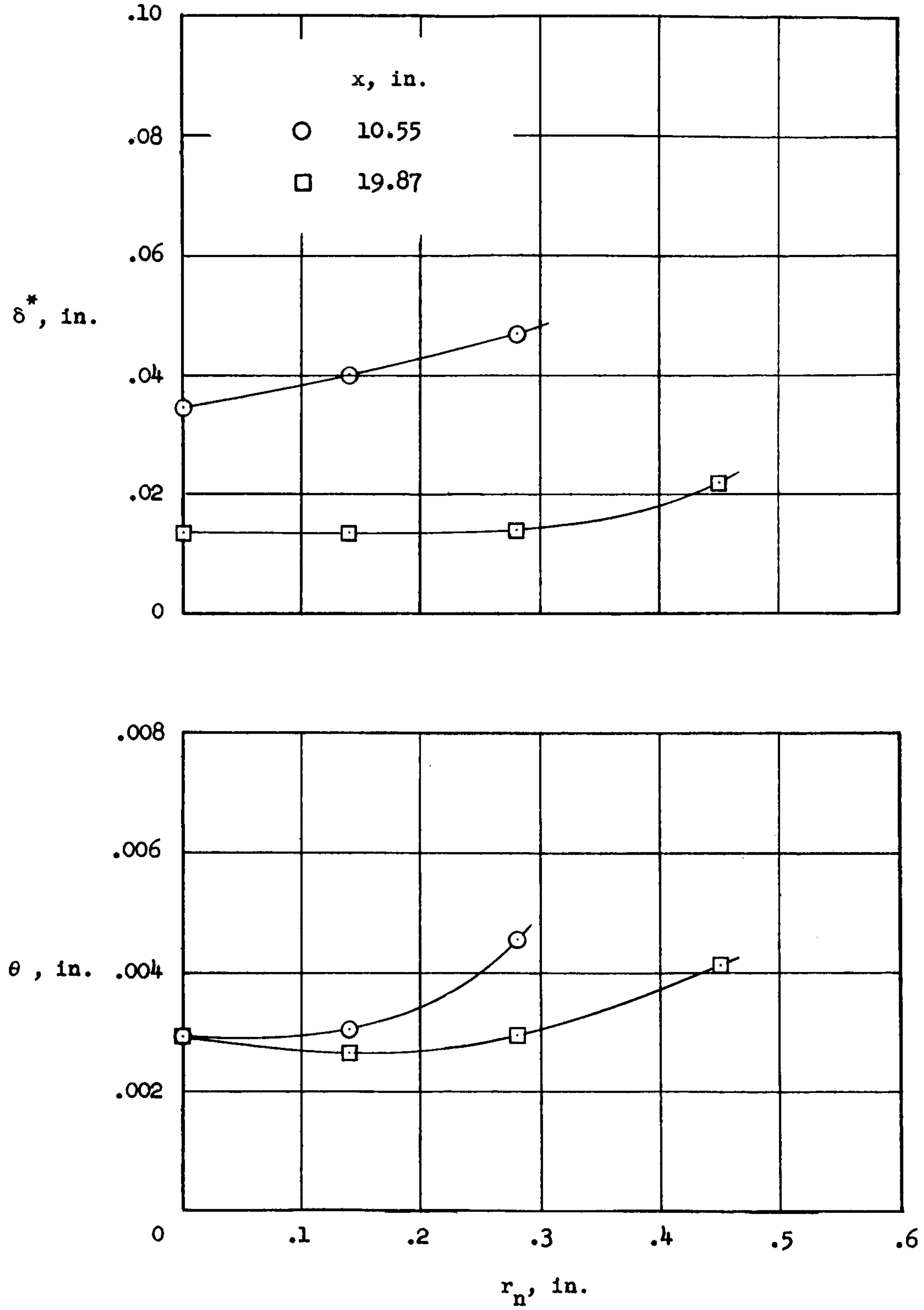

Figure 19.- Effect of nose radius on momentum and displacement thicknesses; $\sigma = 10^{\circ}$; $k = 0$.

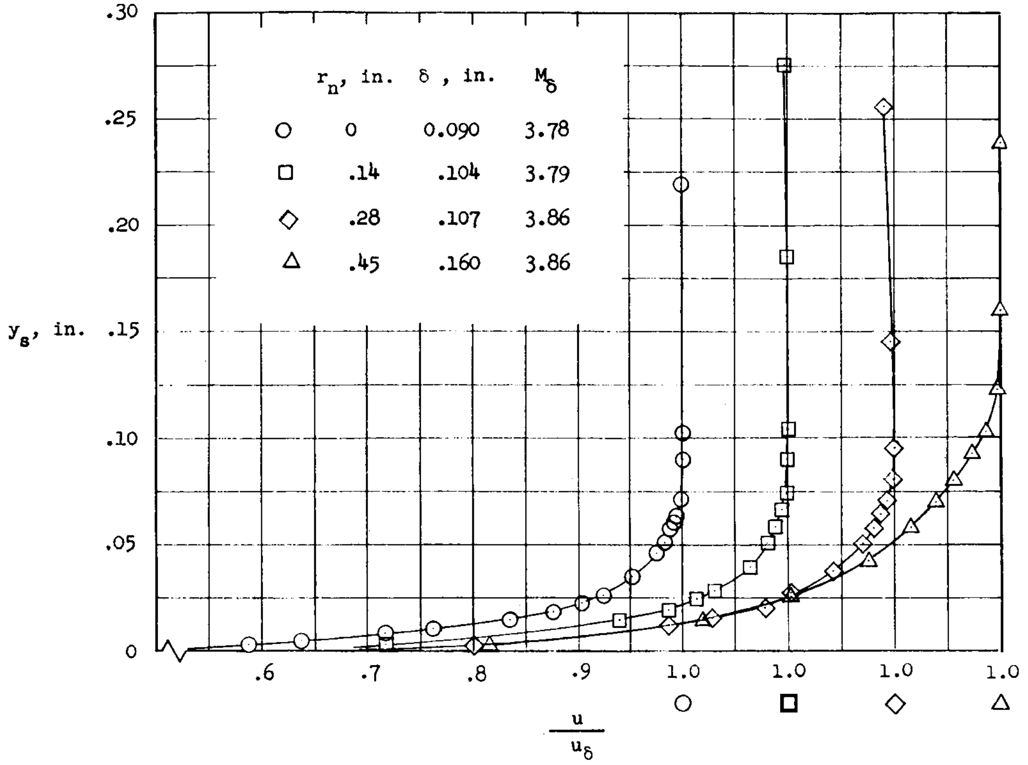

(a) Forward survey station, x = 7.95 in.

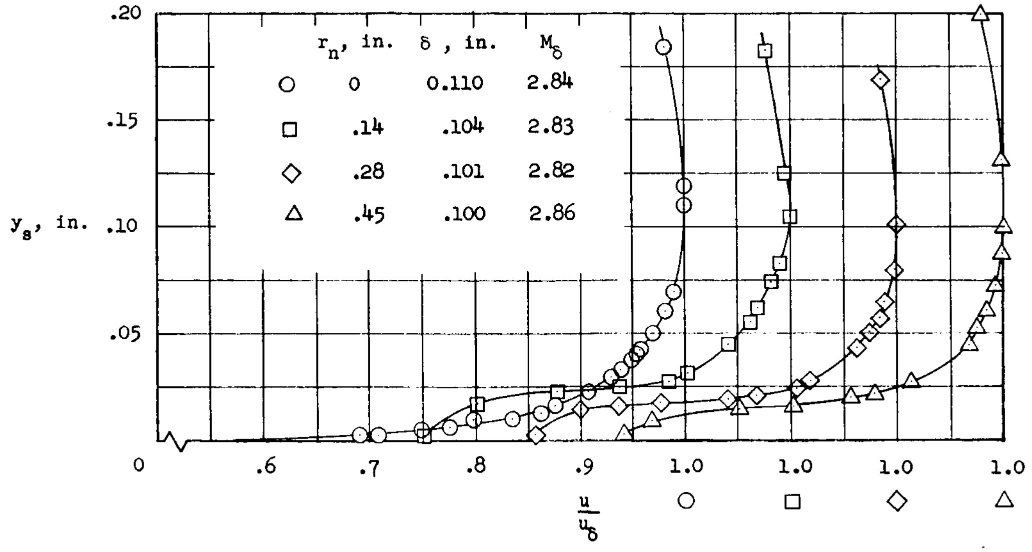

(b) Rearward survey station, x = 11.60 in.

Figure 20.- Boundary-layer velocity profiles; $\sigma = 20^\circ$; k = 0.

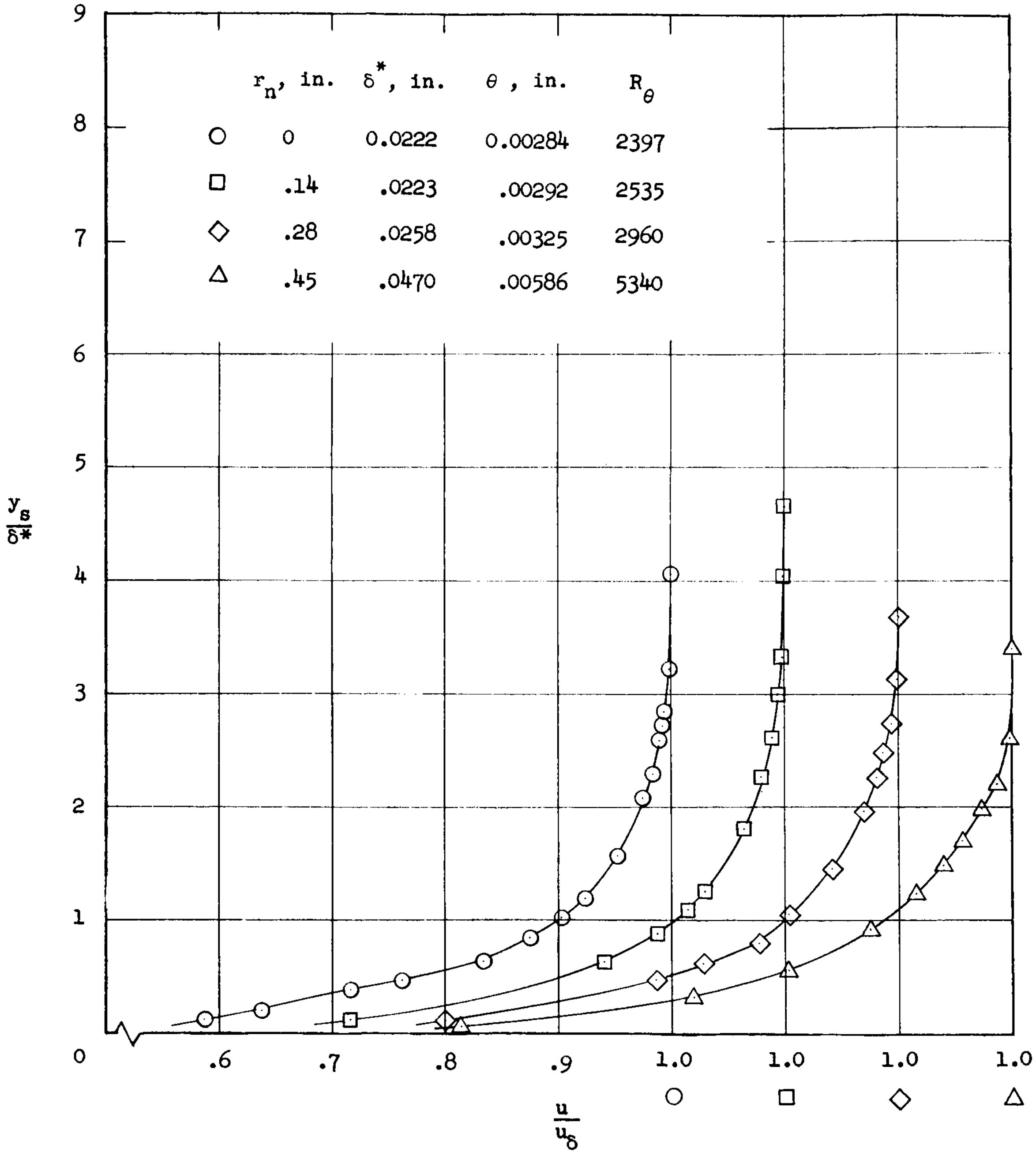

(a) Forward survey station, x = 7.95 in.

Figure 21.- Nondimensional velocity profiles; $\sigma = 20^\circ$; k = 0.

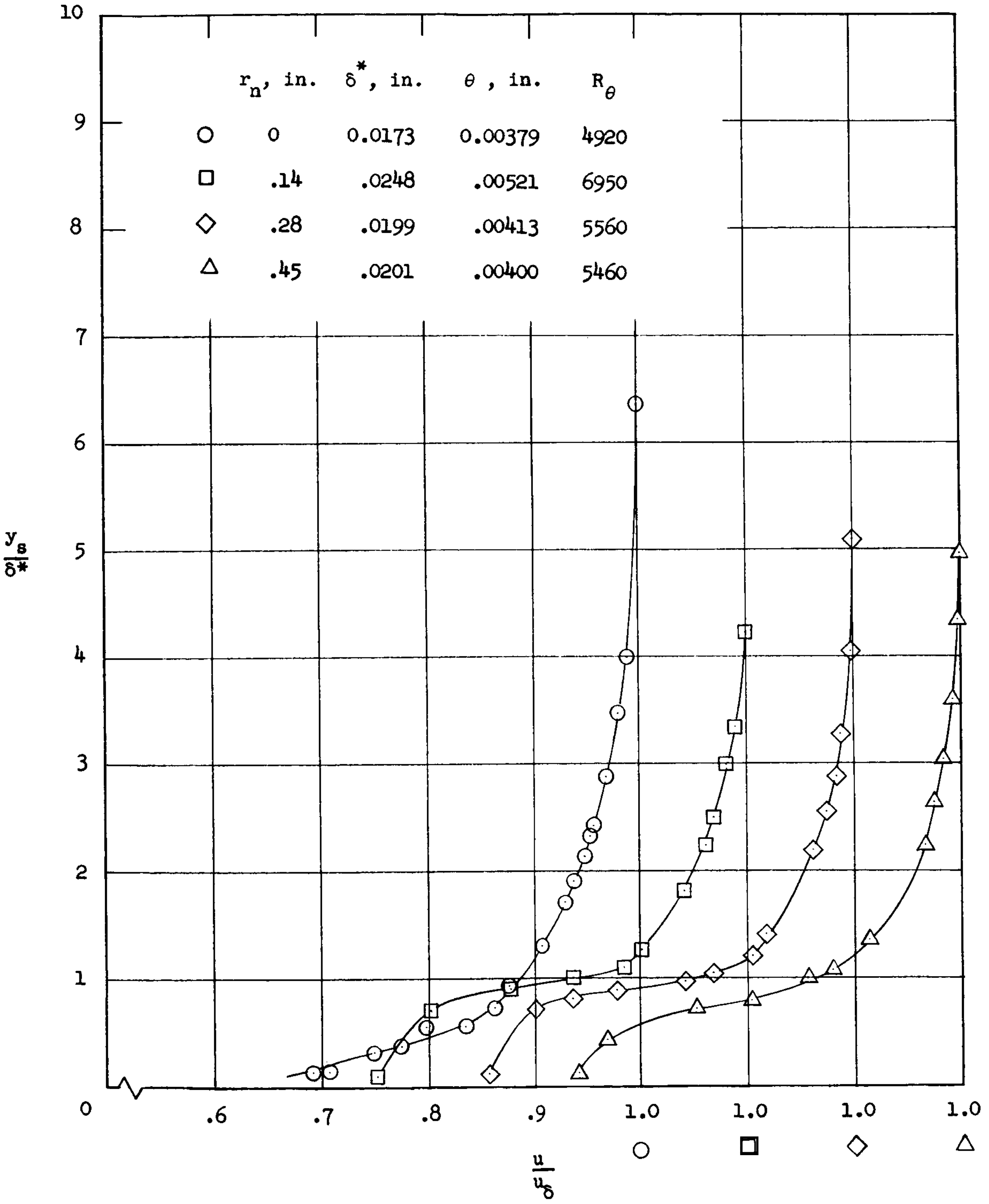

(b) Rearward survey station, x = 11.60 in.

Figure 21.- Concluded.

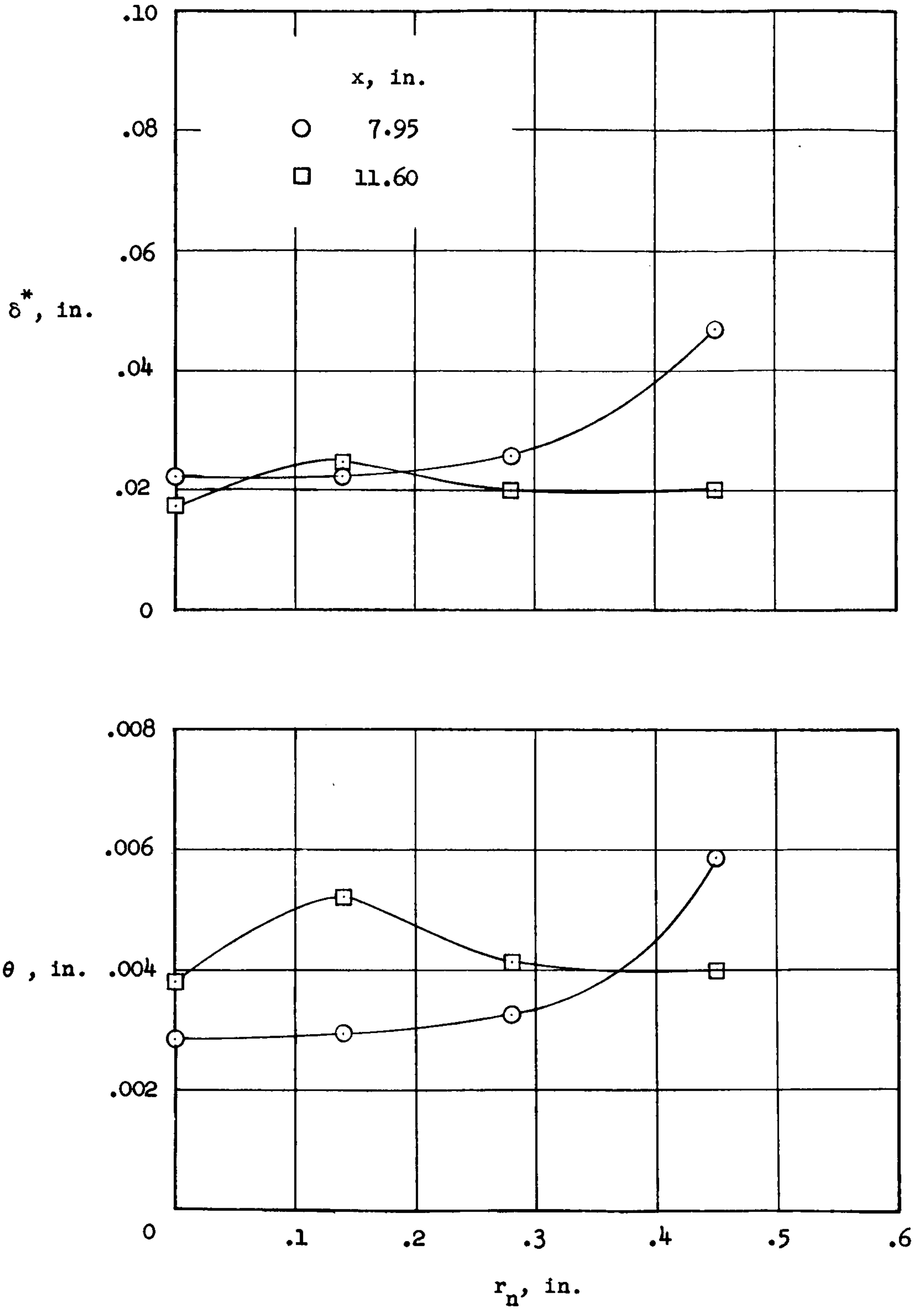

Figure 22.- Effect of nose radius on momentum and displacement thicknesses; $\sigma = 20^\circ$; $k = 0$.

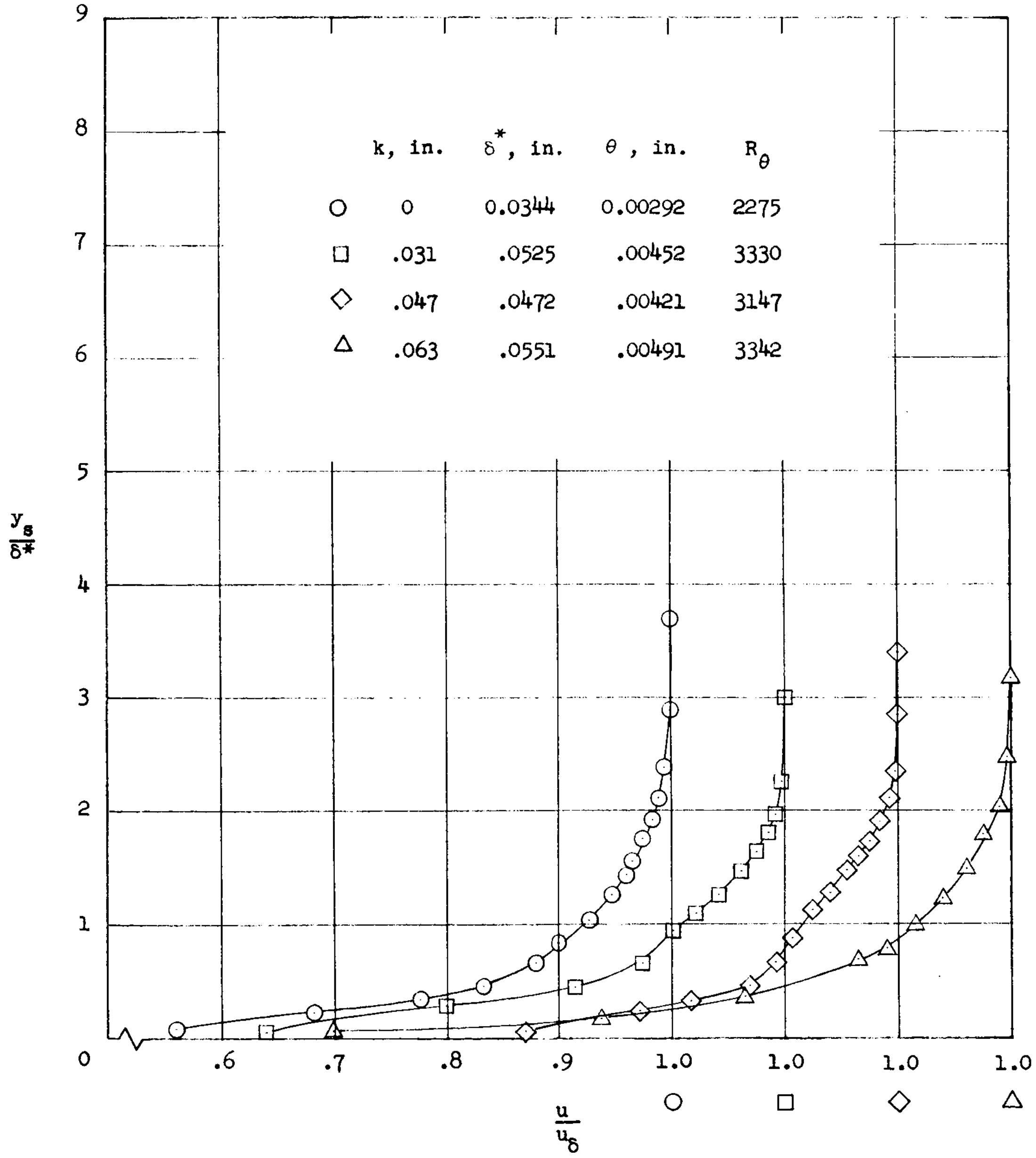

	k, in.	δ^*, in.	θ , in.	R_θ
○	0	0.0344	0.00292	2275
□	.031	.0525	.00452	3330
◇	.047	.0472	.00421	3147
△	.063	.0551	.00491	3342

(a) Forward survey station, x = 10.55 in.

Figure 23.- Nondimensional velocity profiles; $\sigma = 10^{\circ}$; $r_n = 0$.

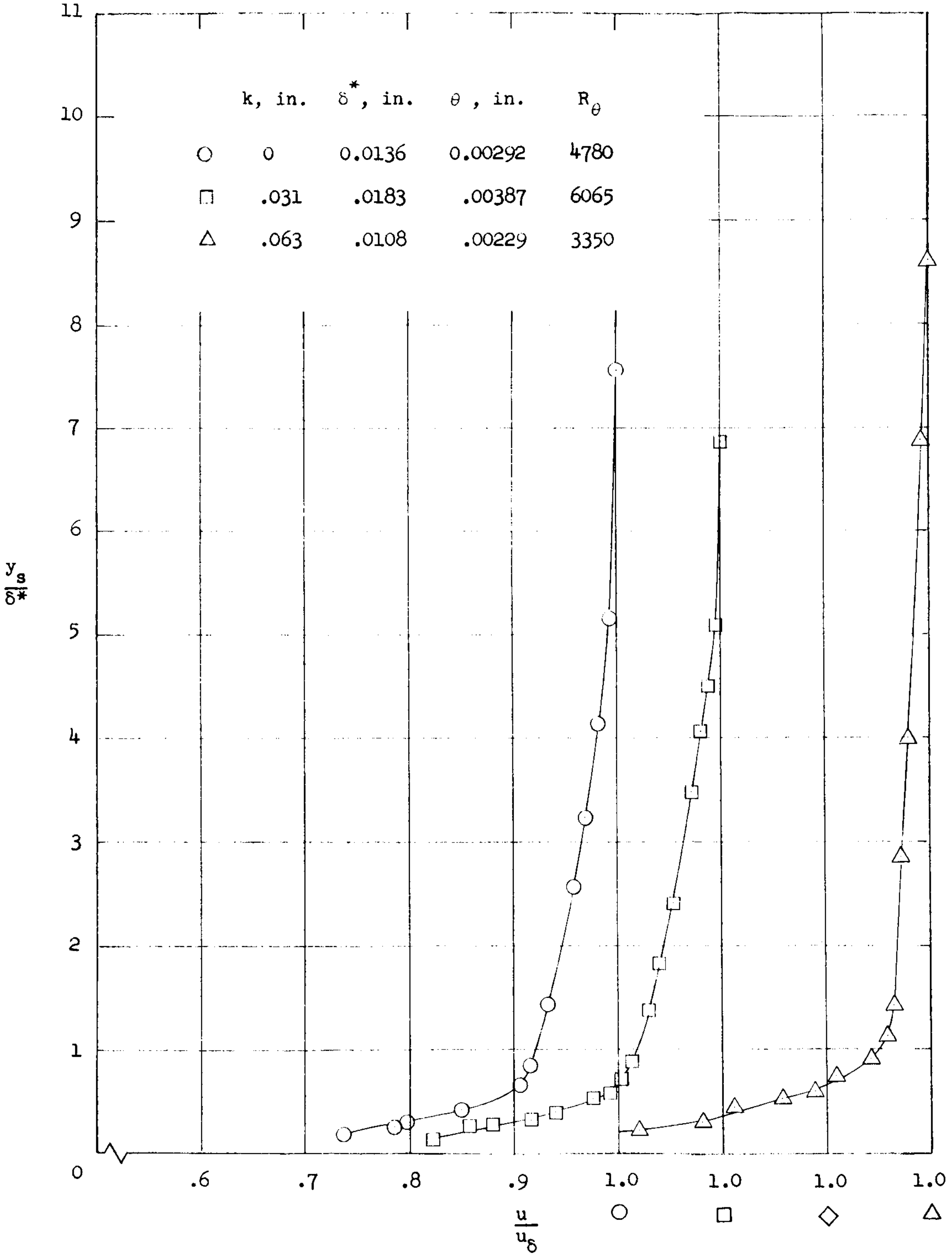

(b) Rearward survey station, x = 19.87 in.

Figure 23.- Concluded.

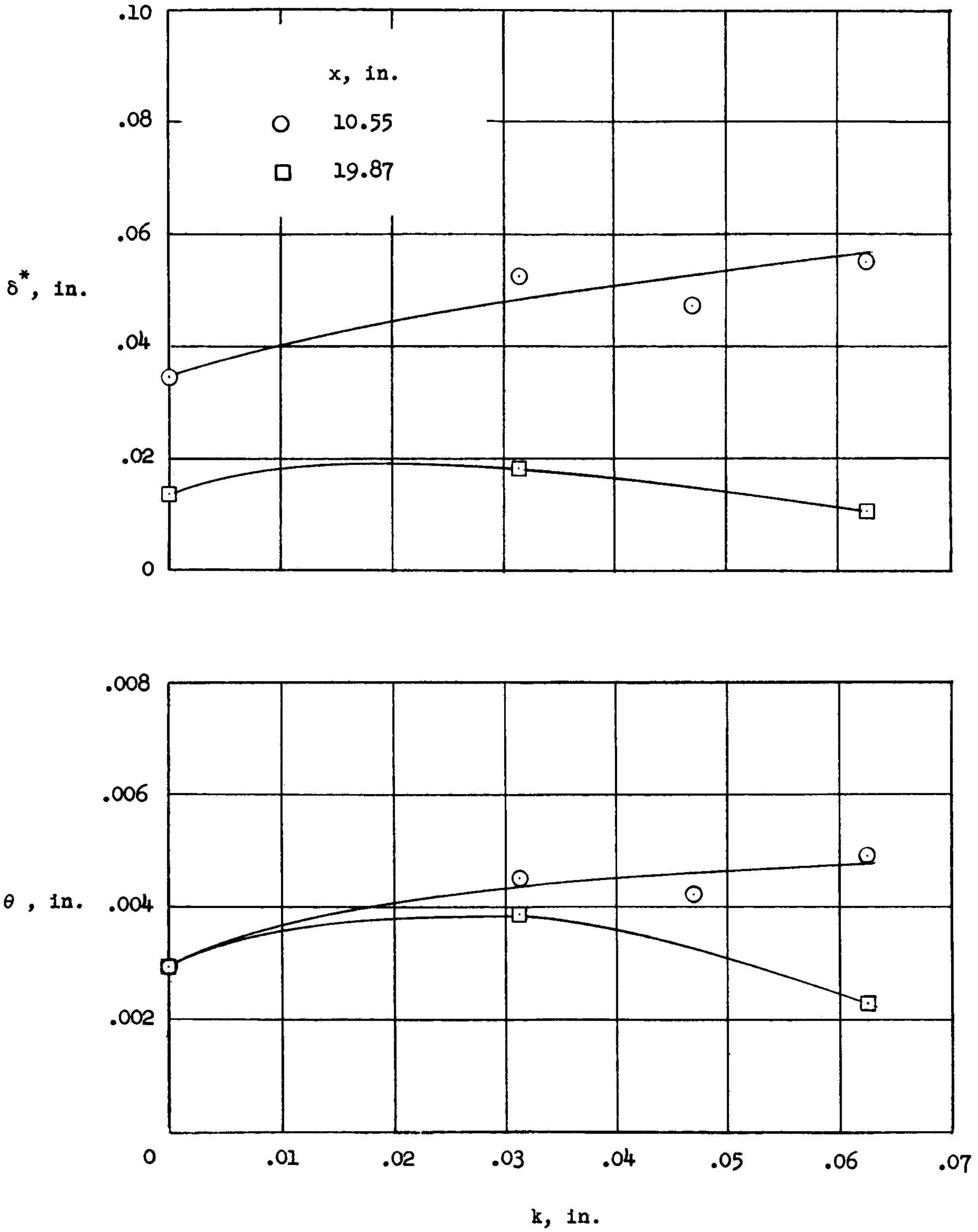

Figure 24.- Effect of roughness size on momentum and displacement thicknesses; $\sigma = 10^{\circ}$; $r_n = 0$.

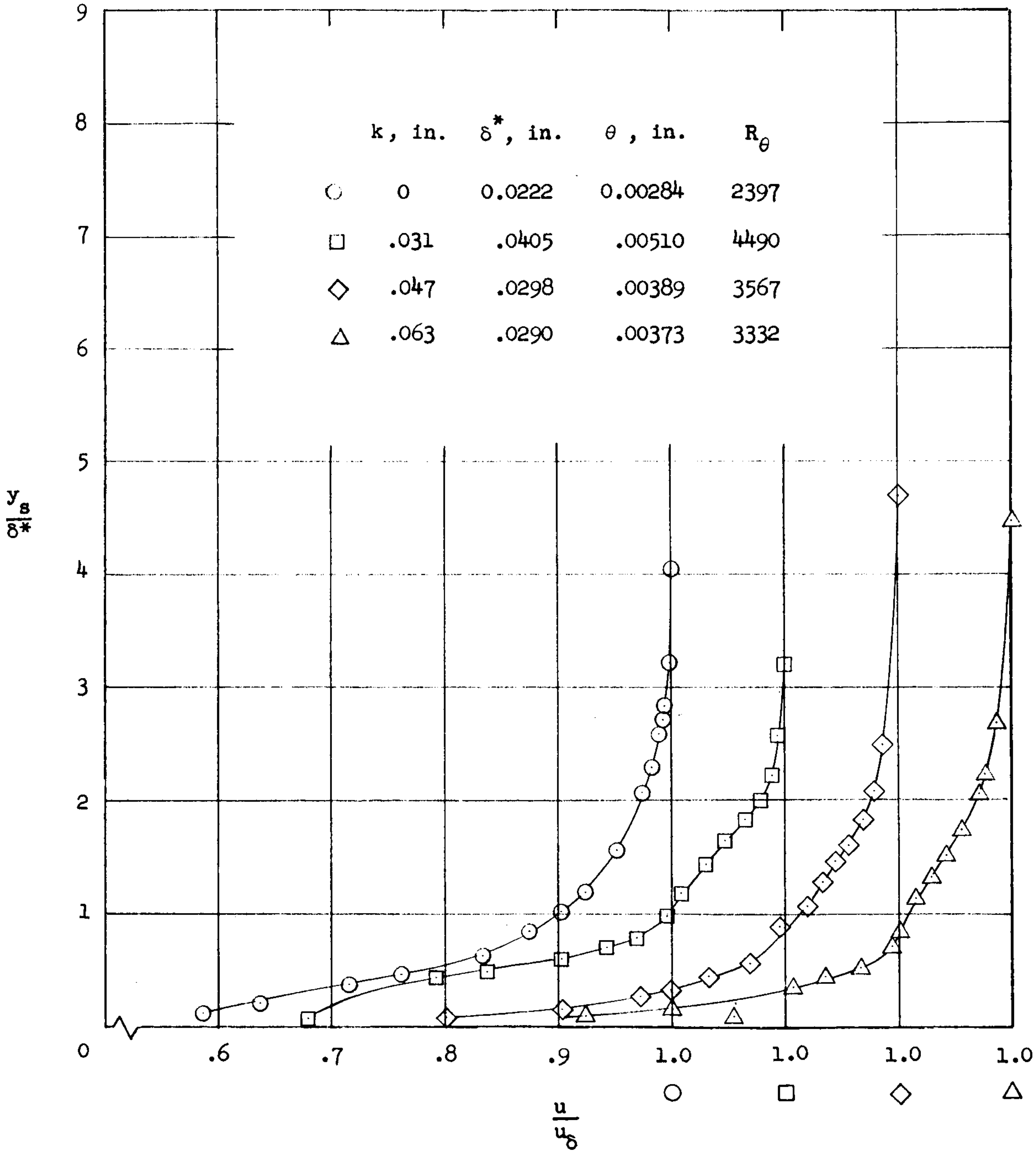

	k, in.	δ^*, in.	θ, in.	R_θ
○	0	0.0222	0.00284	2397
□	.031	.0405	.00510	4490
◇	.047	.0298	.00389	3567
△	.063	.0290	.00373	3332

(a) Forward survey station, x = 7.95 in.

Figure 25.- Nondimensional velocity profiles; $\sigma = 20^\circ$; $r_n = 0$.

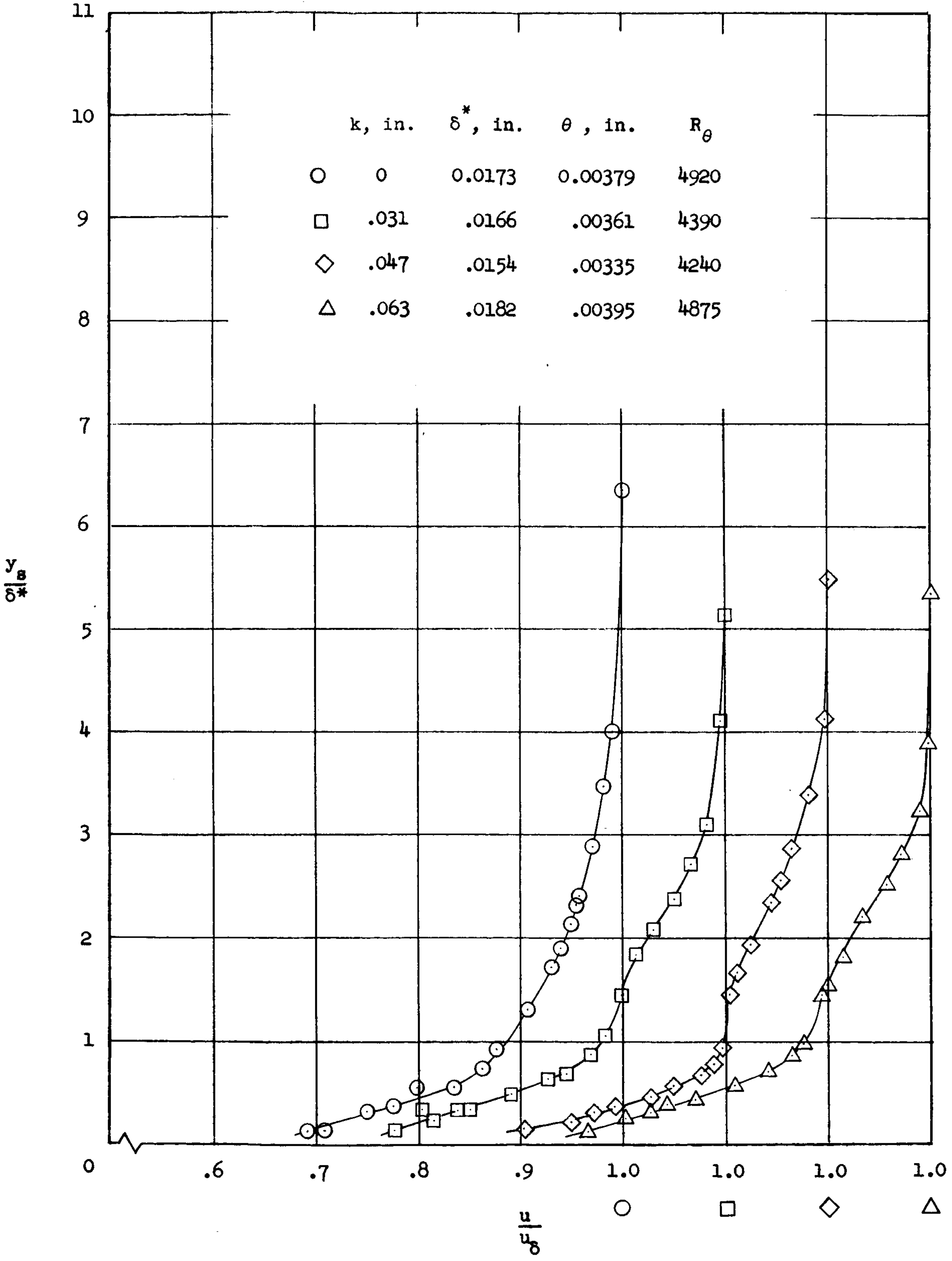

(b) Rearward survey station, x = 11.60 in.

Figure 25.- Concluded.

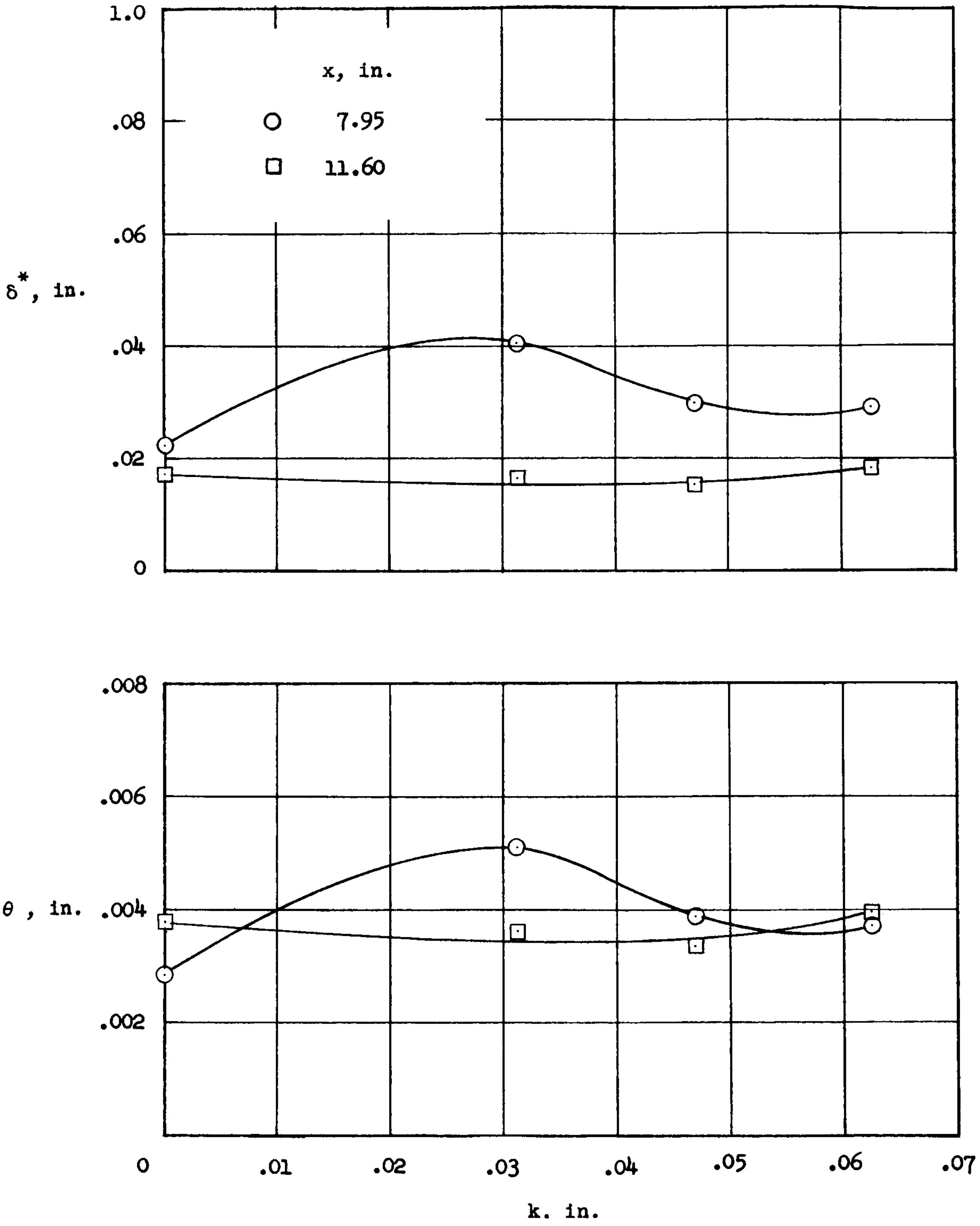

Figure 26.- Effect of roughness size on momentum and displacement thicknesses; $\sigma = 20^{\circ}$; $r_n = 0$.

NASA-Langley, 1965